Engineering high Pockels coefficients in thin-film strontium titanate for cryogenic quantum electro-optic applications

Anja Ulrich[1,2]†, Kamal Brahim[1,3]†, Andries Boelen[1,4]†, Michiel Debaets[1,2], Ahmed Khalil[1,5], Conglin Sun[1,5], Yishu Huang[1,2], Sandeep Seema Saseendran[1], Marina Baryshnikova[1], Paola Favia[1], Thomas Nuytten[1], Stefanie Sergeant[1], Kasper Van Gasse[1,2], Bart Kuyken[1,2], Kristiaan De Greve[1,3,6], Clement Merckling[1,4], Christian Haffner[1]*

[1] Imec; B-3001 Leuven, Belgium.

[2] Department of Information Technology (INTEC), Photonics Research Group, Ghent University; B-9052 Ghent, Belgium.

[3] Department of Electrical Engineering (ESAT), KU Leuven; B-3001 Leuven, Belgium.

[4] Department of Materials Engineering (MTM), KU Leuven; B-3001 Leuven, Belgium.

[5] Department of Physics and Astronomy, KU Leuven; B-3001 Leuven, Belgium.

[6] Proximus Chairs in Quantum Science and Technology, KU Leuven

†Contributing equally.

*Corresponding author. Email: christian.haffner@imec.be

Abstract

Pockels materials are notable for their strong electro-optic interaction and rapid response times and are therefore used extensively in optical communications. Yet many materials optimized for room-temperature operation see their Pockels coefficients reduced at cryogenic temperatures - a major hurdle for emerging quantum technologies. Here, we show that Strontium titanate ($SrTiO_3$) can be engineered to exhibit a Pockels coefficient of 345 pm/V at 20 Hz at cryogenic temperatures – a value twice as high as any other thin-film electro-optic material. By adjusting the stoichiometry, we can increase the Curie temperature and realize a ferroelectric phase yielding a high Pockels coefficient, yet with limited optical losses of decibels per centimeter. Our findings position $SrTiO_3$ as a promising material for cryogenic quantum photonics applications.

Quantum applications, including the transduction of radiofrequency (RF) to optical photons (*1*, *2*) and the high-efficiency detection of photons (*3*) require cryogenic cooling of entire optical systems, including the electro-optic transducers. In the quantum domain, every photon counts – hence the electro-optic materials used need to provide quantum-imposed improved performance characteristics (*4*, *5*) that are maintained at 4 K and below. The improved performance makes shorter electro-optic transducers possible, thus, minimizing photon losses. Only under the assumption that strong and weak Pockels materials can achieve comparably low losses. Said performance of the electro-optic material is best quantified by the Pockels coefficient (r) times the cube of the material's refractive index (*6*) (n) - ergo $n^3 \cdot r$. Together with the losses of the electro-optic material, it is the most important parameter to optimize for electro-optic systems.

Pockels materials (*7–9*) have been optimized extensively for room-temperature data and telecommunication applications (*10*), however their Pockels coefficients reduce significantly at cryogenic temperatures. This behavior can be seen in Fig. 1 A, which compares $n^3 \cdot r$ for various Pockels materials such as lithium niobate ($LiNbO_3$) (*7*, *11*, *12*), organic electro-optic chromophores (OEO) (*9*, *13*) and barium titanate ($BaTiO_3$) (*8*) at room and cryogenic temperatures [Supplementary 5]. One inherent complication in the comparison arises from the fact that Pockels coefficients are tensorial, not scalar. Thus, an effective scalar value (r_{eff}) with the tensor elements being weighted by the strength of optical and RF fields is used.

Miller's empirical rule (*14*): $r \propto (\varepsilon_{\mathrm{r}} - 1) \cdot \delta$ illustrates how the strength of r is intricately linked to a material's ability to break inversion symmetry at the atomic level ($\delta \neq 0$). Thereby it significantly enhances its linear polarizability (ε_r-1), linked to the material's permittivity ε_{r}, by a factor δ (hyperpolarizability) (*14*). From Miller's rule, two strategies can be employed to engineer materials with high Pockels coefficients: using materials with high hyperpolarizability and non-negligible linear polarization, or engineering materials for large linear polarizations and non-zero hyperpolarization. As part of the first strategy, chromophores can be used featuring a large hyperpolarizability via the breaking of electron cloud symmetry; this is achieved by attaching strong acceptor and donor groups to both ends of a π-bridge, while the linear polarization remains in the single digits (*14*). Organic chromophores achieve Pockels coefficients of ~ 140 pm/V at 4 K (*9*), only ~ 10% lower than room-temperature values. To achieve such large hyperpolarizability, the molecule needs to be a few nanometers long. This results in rather narrow bandgaps ~ 1 eV and imposes its own absorption losses (≥ 1 dB/cm) challenge (*14*), (*15*).

As part of the second strategy, ferroelectric complex oxides break symmetry by displacing atoms on angstrom scales – resulting in a non-zero but appreciably lower hyperpolarizability. Instead, their electro-optic response is driven by a large permittivity in the RF spectrum, originating from material resonances such as space-charge regions, dipolar relaxation, and phononic lattice resonances. However, only the latter provides the gigahertz bandwidth needed for quantum applications. For classical communication applications, complex oxides such as $LiNbO_3$ and $BaTiO_3$ feature both better material stability (*16*), (*17*) and lower optical losses (*14*), (*15*) compared to organic chromophores.

Therefore, the question becomes how can such permittivity engineering be realized? From symmetry configurations, ferroelectric phases are expected to be required for non-zero hyperpolarizability. When cooling down around the paraelectric to the ferroelectric phase transition, the phononic modes tend to soften resulting in a larger permittivity. Hence, by working below but 'close' to the Curie temperature (T_C), a high permittivity (Fig. 1 C) and thus a strong electro-optic effect could be expected. This engineering must also balance the tradeoff with losses naturally occurring at the transition (Kramer-Kronig (*6*)). Of the known complex oxides, $LiNbO_3$

is a prime Pockels material example in optical communications due to its very low (sub-decibel per meter) absorption losses and proven reliability (*12*). However, due to the relative stiffness of the phononic mode of $LiNbO_3$ ($T_C \approx 1200$ K), its resonant enhancement is rather limited (i.e. $\varepsilon_r \approx 30$), and the resulting electro-optic coefficient of 24 pm/V remains rather moderate at cryogenic temperatures (*7*). In contrast, $BaTiO_3$ features a T_C of 400 K offering a high permittivity of a few thousand at room temperature – boosting r_{eff} to 520 ± 20 pm/V (*8*). Unfortunately, this does not persist at cryogenic temperatures as the phononic modes stiffen and $BaTiO_3$ also undergoes several crystal phase transitions when cooling down, resulting in a reduced $r_{\text{eff}} \approx 170 \pm 20$ pm/V (*18*).

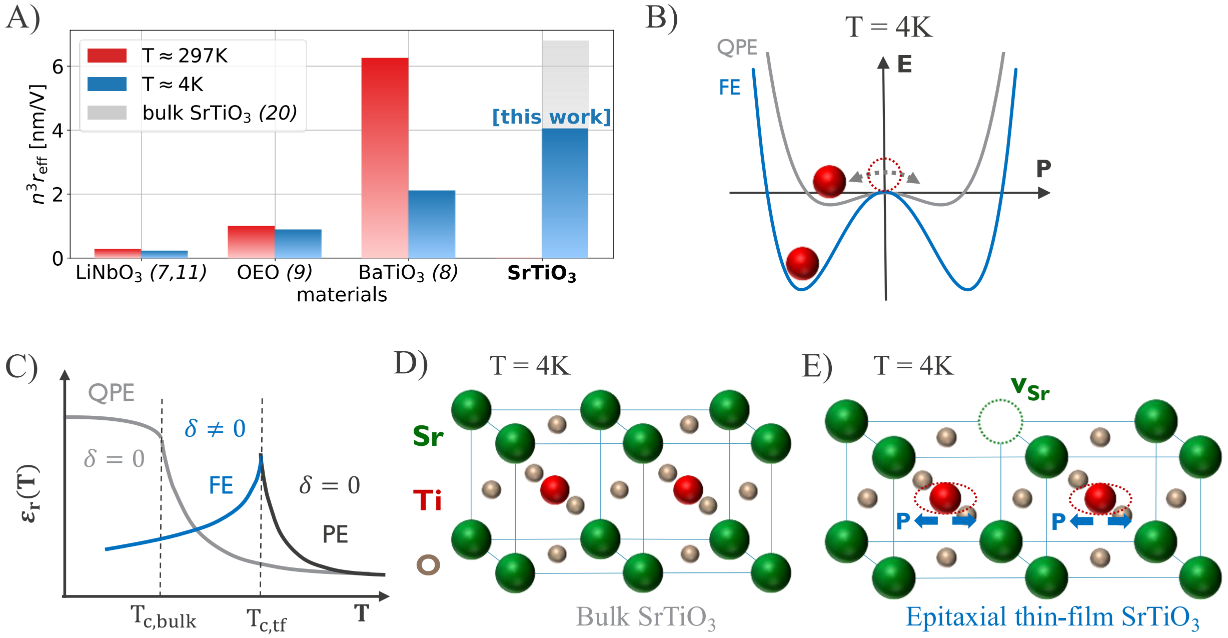

Fig. 1. Relationship between Pockels coefficient, ferroelectric phase transition and crystal structure. (A) Reported effective electro-optic strength of known thin-film Pockels materials on silicon dioxide. $SrTiO_3$ features the largest cryogenic coefficient, highlighting its potential for quantum applications. **(B)** Difference in energy vs. polarization potential of Ti in the quantum paraelectric (QPE) and ferroelectric (FE) phase of $SrTiO_3$. Quantum fluctuations prevent the localization of the Ti atom, and the formation of a proper FE transition. **(C)** Permittivity vs. temperature schematics showing the effect of mode softening around the Curie temperature (T_C) for the thin-film (tf) case (FE) and bulk $SrTiO_3$ case (QPE). The hyperpolarizability indicates symmetric ($\boldsymbol{\delta} = \mathbf{0}$) or broken symmetry ($\boldsymbol{\delta} \neq \mathbf{0}$) phases. **(D)** Centrosymmetric crystal structure of bulk $SrTiO_3$. **(E)** Inversion symmetry broken crystal structure of thin-film $SrTiO_3$ resulting in ferroelectric behavior.

For cryogenic applications, materials with T_C close to the operation temperature might seem suitable; however, this at first appears impractical. Strontium titanate ($SrTiO_3$) with a T_C of ≈ 37 K exemplifies inherent issues with low-T_C materials as quantum fluctuations hinder a ferroelectric phase transition (*19*). In the so-called quantum paraelectric phase, the ground state of the Ti atom is not localized within a potential minimum (Fig. 1 B). This results in a high polarizability as the Ti atom can be strongly displaced by weak fields, leading to high polarizability but no broken symmetry ($\delta = 0$), resulting in a zero Pockels coefficient. Thus, quantum paraelectric materials like $SrTiO_3$ were not considered viable Pockels materials until now.

We challenge this conventional understanding by engineering thin-film $SrTiO_3$ to break its symmetry. $SrTiO_3$ was epitaxially grown on silicon with subsequent wafer bonding onto a silicon dioxide substrate. The slight Ti-rich flavor of the film in combination with strain increases the T_C to 100 K, **high** enough to negate the effect of quantum fluctuations and thereby enable a proper, symmetry-breaking phase (Fig. 1 E). Yet T_C is still **low** enough to benefit from the high permittivity due to lattice resonances. Recently in isotopically doped quantum paraelectric $SrTiO_3$ a large quadratic electro-optic Kerr effect was observed under DC bias (*20*); with an equivalent Pockels coefficient of 1150 pm/V. Our study on wafer-scale thin-film $SrTiO_3$ in combination with the large quadratic electro-optic Kerr effect observed in the bulk crystal underscores the potential of $SrTiO_3$ to surpass traditional Pockels materials in cryogenic electro-optic performance.

Engineered symmetry breaking and ferroelectricity

High-quality epitaxial $SrTiO_3$ films were grown by molecular beam epitaxy (MBE) on 200 mm (001)-oriented Si wafers (*21*). Rutherford backscattering spectroscopy (RBS) determined a stoichiometry of Sr/Ti = 0.96 ± 0.03. We expect this slightly Ti-rich stoichiometry to provide a good trade-off between symmetry breaking (*22*) while still preserving a highly crystalline structure, the latter imposing growth conditions around Sr/Ti = 1. Post-growth, the wafer was bonded onto a low refractive index SiO_2 box to optically isolate the $SrTiO_3$ film from the high refractive index silicon substrate [Supplementary 1]. Additionally, high-temperature oxygen annealing treatments were performed to reduce the oxygen vacancy concentration and further increase the film's crystallinity (*23*). The thin-film crystallinity was quantified via x-ray diffraction (XRD) and benchmarked against commercial bulk references by comparing the full width at half maximum (FWHM) data of the ω-scan from the $SrTiO_3$ (002) diffraction peak. Fig. 2 A) shows the FWHM wafer map featuring an average FWHM of 0.11 ± 0.02, while bulk $SrTiO_3$ (001) substrates (1 x 1 cm^2) showed a FWHM of 0.022 ± 0.007°. Transmission electron microscopy (TEM) analysis confirmed the epitaxial nature of the $SrTiO_3$ layer, revealing a sharp $SiO_2/SrTiO_3$ interface (Fig. 2 B). Threading dislocations, which are common in heteroepitaxial thin films, were observed to extend vertically through the full $SrTiO_3$ layer, from the substrate interface to the top surface. These can act as space charge regions, disrupt lattice uniformity, and increase conductivity.

Impedance spectroscopy was used to directly measure the large cryogenic RF permittivity. These measurements were further extended to encompass a broad temperature range from 5 K to 300 K, and for frequencies spanning from 100 kHz to 1 GHz, using specially designed interdigitated capacitors. Upon increasing the temperature from 5 K to room temperature, the permittivity peaks at 100 K before dropping to ~ 600 at room temperature (Fig. 2 D). Such behavior is normally associated with a paraelectric (at high temperature) to ferroelectric (low temperature) phase transition around T_C. The phase transition breaks the crystal symmetry and gives rise to a non-zero Pockels coefficient. While pure ferroelectric materials typically feature a sharp phase transition at T_C, our $SrTiO_3$ film demonstrates a broader continuous transition from the paraelectric to ferroelectric phase during cooldown. Furthermore, we observe a slight lowering of permittivity with frequency from 2700 at 100 kHz to 2500 at 1 GHz (Fig. 2 C). Such broadening of the phase transition and reduction in permittivity over frequency is commonly associated with relaxor ferroelectric behavior - linked to polar nanoregions (*24*, *25*). Polarizing and depolarizing these polar nanoregions adds a contribution to the relative permittivity at low frequencies. Our measurement indicates that this low-frequency effect is limited to ≈ 10% of the total permittivity. As the Pockels coefficient scales with permittivity, our data suggests that the high Pockels coefficient of $SrTiO_3$ can be sustained up to GHz operations.

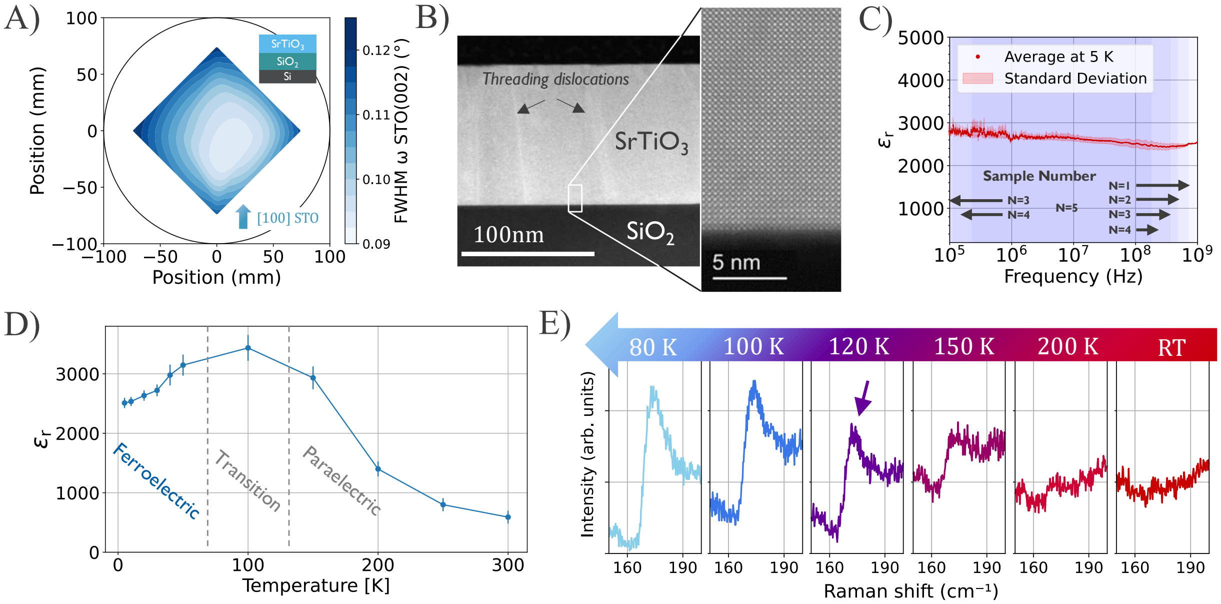

Fig. 2. $SrTiO_3$ thin-film crystal quality, permittivity and evidence of ferroelectricity. (A) FWHM of the $SrTiO_3$ (002) ω-scan mapped over a full 200 mm wafer, showing good uniformity of the crystal quality. **(B)** Cross-sectional TEM of the epitaxial 105 nm $SrTiO_3$ thin film. **(C)** Cryogenic permittivity ($\boldsymbol{\varepsilon}_r$) vs. frequency response from 100 kHz to 1 GHz, showing a large but slowly decreasing permittivity which drives the strong Pockels coefficient over a broad frequency range up to 1 GHz. N represents the number of samples. **(D)** Temperature dependence of $\boldsymbol{\varepsilon}_r$ at 100 MHz showing a paraelectric to (symmetry broken) ferroelectric phase transition around 100 K. **(E)** Temperature-dependent Raman spectroscopy. Upon cooling down from room temperature (RT), a Raman signal at ~ 173 cm^{-1} appears indicating a symmetry breaking.

To verify the $SrTiO_3$ ferroelectric phase transition, temperature-dependent Raman spectroscopy was performed to measure the phononic lattice modes (Fig. 2 E). For $SrTiO_3$ in the (quantum) paraelectric phase, first-order Raman scattering (involving only one phonon) is symmetry forbidden as the unit cell is centrosymmetric. Upon cooling, a peak at ~ 173 cm^{-1} becomes active, corresponding to lattice vibrations. This feature is attributed to the longitudinal component of the so-called Slater mode and transversal component of the Last mode, both oscillating at 5.2 THz. The Slater mode describes mutually opposite vibrational displacements of the Ti and O atoms along the c-axis (axis of Ti displacement), whereas the Last mode corresponds to the coupled vibrations of the TiO_6 octahedra and the Sr ions (*24*, *25*). The (gradual) appearance of this peak below 200 K indicates a (gradual) breaking of the crystal's centrosymmetry, further supporting our observations of relaxor ferroelectric behavior (*26*). Room-temperature lattice parameters of 3.905 ± 0.005 Å (in-plane) and 3.901 ± 0.005 Å (out-of-plane) suggest a cubic-like $SrTiO_3$ unit cell that mimics bulk properties (a_{bulk} = 3.905 Å). However, due to a factor three difference in thermal expansion coefficients (CTE) between film and substrate, cooling down the sample can induce a strain of ~ 0.18% [Supplementary 2]. This can contribute to the $SrTiO_3$ ferroelectric phase transition at 100 K (*27*). Conversely, the resulting strain may still be partially relaxed due to dislocations within the film, hence further investigation is needed to estimate the effective $SrTiO_3$ strain at cryogenic temperatures.

Electro-optic interaction strength and bandwidth

The symmetry breaking phase of $BaTiO_3$ or $SrTiO_3$ is accomplished by the displacement of the Ti atom within a unit cell. This displacement can randomly occur in four directions, resulting in a net zero macroscopic electro-optic effect. Applying a poling field aligns the atomic displacement and results in a macroscopic electro-optic response. To investigate the poling behavior of our thin films and quantify the electro-optic response strength, a Mach-Zehnder interferometer (MZI) was designed based on polymethyl methacrylate (PMMA) loaded waveguides in combination with chromium/platinum electrodes. PMMA and the SiO_2-substrate can be considered electro-optically inert, ensuring that the observed effects are primarily due to the 43% light confinement within the $SrTiO_3$ layer (Fig. 3 A). The measured waveguide propagation losses are dominated by coupling leakage to substrate modes; quantifying these, we estimate that the material losses of our $SrTiO_3$ films are below 5.5 dB/cm [Supplementary 6]. These losses are in contrast to previous reports and conventional assumption that associates thin-film $SrTiO_3$ layers with high optical losses (*28*). Applying an electric field (E_{AC}) induces a phase change of the light propagating in the waveguide ($\Delta\psi \propto v_{\mathrm{pol}} \cdot r_{\mathrm{eff}} \cdot E_{\mathrm{AC}}$). Here, v_{pol} describes the degree of Ti atoms being displaced in the same direction and can reach values of ± 1 for perfect poling. The designed MZI (Fig. 3 B) translates the electric field induced phase changes into a modulation of the optical power by means of destructive and constructive interference between light propagating in the modulated and unmodulated arm. Fig. 3 C shows a strong oscillation of power (bottom) versus drive field (top) indicating a large electro-optic effect. In detail a voltage change of 0.084 V/μm results in a π phase shift corresponding to a $V_\pi L \approx 1.04 \pm 0.08$ Vcm [Supplementary 4.2].

Fig. 3 D shows a hysteresis behavior of the extracted phase versus applied field. This is indeed indicative of a ferroelectric phase in the thin-film $SrTiO_3$ (*29*). The vertical dashed lines indicate the coercive field at which enough energy is provided to switch back previously poled domains to generate a net zero phase change. r_{eff} is extracted from the slope of Fig. 3 D) [Supplementary 4.2]. For fields above the coercive field, the poling function becomes a constant and r_{eff} in Fig. 3 E should flatten out. However, under strong fields a drop of r_{eff} can be observed [Supplementary 4.2] which we attribute to a ~ 60% lowering of the permittivity under strong fields. This behavior is in line with what has been reported for ferroelectrics (*25*). Therefore, the achievable electro-optic coefficient will depend on the operation conditions (i.e. bias and ac voltages) and reaches values up to 345 ± 10 pm/V under small bias at 20 Hz, dropping to 140 ± 3 pm/V with a 1.6 V/μm bias field. The latter value was confirmed by performing a 1 kHz small signal modulation [Supplementary 4.3]. Quantum paraelectric $SrTiO_3$ (*20*) shows a similar trend, but a stronger drop is expected for high fields of 1 V/μm as the permittivity reduces by a factor of ten (*30*). Therefore, devices based on $SrTiO_3$ in the ferroelectric phase might be better suited for applications that require higher drive voltages to enable shorter devices and thus keep optical losses at a minimum (*5*).

Due to bandwidth limitations in our cryogenic setups, we used an indirect small-signal method to infer the electro-optic frequency response. This method uses the effect that an applied ac signal has on the average optical power, resulting in a drop with respect to MZI's on-point (P_{on}) (inset of Fig. 3 F). This drop is proportional to the electro-optic strength of the Pockels material. Fig. 3 E shows that the drop in optical power is unaffected by an increase in ac modulation frequency, indicating a constant modulation up to 1 MHz [Supplementary 4.4]. The electro-optic bandwidth measurement in combination with the up to 1 GHz permittivity measurements indicates the absence of sub-GHz resonances and promises high-frequency operation of $SrTiO_3$. The reduced response at low frequencies (< 20 Hz) prevented any DC bias experiments [Supplementary 4.5]. This low-frequency response might be due to an oxygen vacancy-related mechanism that effectively screens bias fields. Further investigation is needed to determine if this is related to non-stoichiometric $SrTiO_3$ near the electrodes or oxidation of the Cr-$SrTiO_3$ interface (*31*).

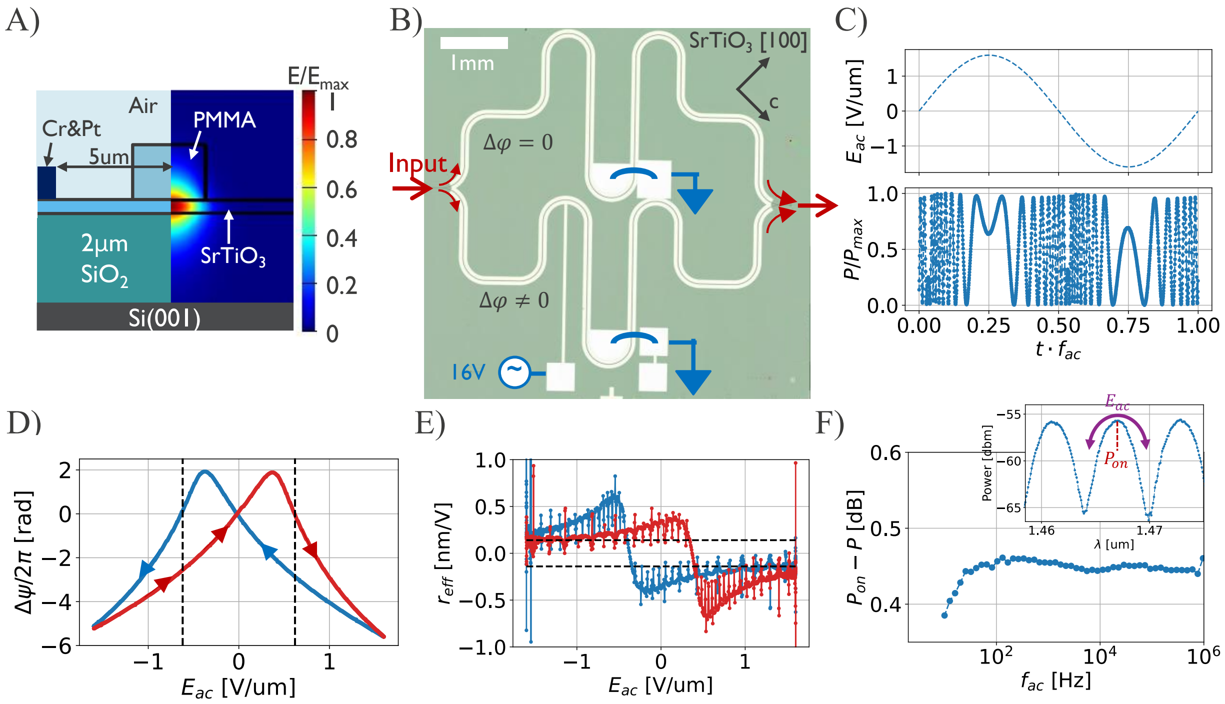

Fig. 3. Summary of electro-optic measurements and effective Pockels coefficient. (A) (left) schematic cross section of the device, (right) simulated optical mode profile. **(B)** Top view of the meandered MZI with the ferroelectric crystal structure indicated by the black arrows. The bottom arm is modulated by an electrical signal and destructively/constructively interferes with the upper arm, allowing to track the phase change by measuring the transmitted power. (**C**) One period of the applied 20 Hz, 1.6 V/µm drive signal (top) and the optical output power response of the MZI (bottom). (**D**) The induced phase change in the lower MZI arm vs. applied electric field, indicative of so-called poling behavior (voltage sweep downwards (blue) and upward wards (red)). Vertical lines mark the coercive field 0.6 ± 0.05 V/µm. **(E)** Pockels coefficient $\boldsymbol{r}_{\mathbf{eff}}$ extracted from D). The reported 345 ± 10 pm/V at 20 Hz corresponds to the (remanent) zero field value in the upward direction (red). **(F)** Electro-optic bandwidth measurement. Frequencies below 20 Hz show a reduced response – potentially caused by a DC screening effect.

Outlook

We have demonstrated a high Pockels effect in thin-film $SrTiO_3$ at 4 K, driven by its ferroelectric properties. And while optical losses of a few dB/cm are significantly higher than $LiNbO_3$ losses, $BaTiO_3$, the older sibling of $SrTiO_3$, has already demonstrated loss reduction to 0.2dB/cm (*32*). Like many other novel photonic materials, the capability to integrate $SrTiO_3$ with existing photonics platforms based on silicon nitride or silicon will be crucial to provide practical relevance. And while lithium niobate currently poses contamination risks in large-scale semiconductor and photonics fabrication (*33*), we already processed the $SrTiO_3$ wafer in imec's 200 mm photonic pilot line to perform the wafer bonding step.

References and Notes

1. J. D. Witmer *et al.*, A silicon-organic hybrid platform for quantum microwave-to-optical transduction. *Quantum Sci. Technol.* **5**, 034004 (2020).
2. M. Mirhosseini *et al.*, Superconducting qubit to optical photon transduction. *Nature* **588**, 599–603 (2020).
3. A. W. Elshaari *et al.*, Hybrid integrated quantum photonic circuits. *Nat. Photonics* **14**, 285–298 (2020).
4. H. Aghaee Rad *et al.*, Scaling and networking a modular photonic quantum computer. *Nature*, doi: 10.1038/s41586-024-08406-9 (2025).
5. G. Moody *et al.*, 2022 Roadmap on integrated quantum photonics. *J. Phys. Photonics* **4**, 012501 (2022).
6. R. W. Boyd, *Nonlinear Optics* (Academic Press, Burlington, MA, 3rd ed., 2008).
7. D. Zhu *et al.*, Integrated photonics on thin-film lithium niobate. doi: 10.48550/ARXIV.2102.11956 (2021).
8. F. Eltes *et al.*, An integrated optical modulator operating at cryogenic temperatures. *Nat. Mater.* **19**, 1164–1168 (2020).
9. D. Bisang *et al.*, Plasmonic Modulators in Cryogenic Environment Featuring Bandwidths in Excess of 100 GHz and Reduced Plasmonic Losses. *ACS Photonics* **11**, 2691–2699 (2024).
10. A. Boes *et al.*, Lithium niobate photonics: Unlocking the electromagnetic spectrum. *Science* **379**, eabj4396 (2023).
11. C. Herzog *et al.*, Electro-optic behavior of lithium niobate at cryogenic temperatures. *Opt. Commun.* **281**, 793–796 (2008).
12. A. Shams-Ansari *et al.*, Reduced material loss in thin-film lithium niobate waveguides. *APL Photonics* **7**, 081301 (2022).
13. HLD - Organic Non-linear Optical (NLO) Material with High Electro-optic Effects (2021). https://www.nlmphotonics.com/wp-content/uploads/2021/09/nlm-bi-fold-8-11_9-21-1.pdf.
14. L. R. Dalton *et al.*, *Organic Electro-Optics and Photonics: Molecules, Polymers and Crystals* (Cambridge University Press, ed. 1, 2015; https://www.cambridge.org/core/product/identifier/9781139043885/type/book).
15. S. Feng *et al.*, Organic Electro-Optic Materials with High Electro-Optic Coefficients and Strong Stability. *Molecules* **29**, 3188 (2024).

16. Y. Tominari *et al.*, Photostability of organic electro-optic polymer under practical high intensity continuous-wave 1550 nm laser irradiation. *Jpn. J. Appl. Phys.* **60**, 101002 (2021).

17. H. Xu *et al.*, Recent Progress in Design of Organic Electro-optic Materials with Ultrahigh Electro-optic Activities†. *Chin. J. Chem.* **40**, 3001–3012 (2022).

18. A. Karvounis *et al.*, Barium Titanate Nanostructures and Thin Films for Photonics. *Adv. Opt. Mater.* **8**, 2001249 (2020).

19. K. A. Müller *et al.*, SrTi O 3 : An intrinsic quantum paraelectric below 4 K. *Phys. Rev. B* **19**, 3593–3602 (1979).

20. C. P. Anderson *et al.*, Quantum critical electro-optic and piezo-electric nonlinearities. arXiv arXiv:2502.15164 [Preprint] (2025). https://doi.org/10.48550/arXiv.2502.15164.

21. A. Boelen *et al.*, Stoichiometry and Thickness of Epitaxial SrTiO$_{3}$ on Silicon (001): an Investigation of Physical, Optical and Electrical Properties. arXiv [Preprint] (2024). https://doi.org/10.48550/ARXIV.2412.07395.

22. K. T. Kang *et al.*, Ferroelectricity in SrTiO3 epitaxial thin films via Sr-vacancy-induced tetragonality. *Appl. Surf. Sci.* **499**, 143930 (2020).

23. M. Baryshnikova *et al.*, Impact of Cationic Stoichiometry on Physical, Optical and Electrical Properties of SrTiO3 Thin Films Grown on (001)-Oriented Si Substrates. *Materials* **17**, 1714 (2024).

24. V. Dwij *et al.*, Fano resonance and relaxor behavior in Pr doped SrTiO3: A Raman spectroscopic investigation. *Phys. B Condens. Matter* **620**, 413265 (2021).

25. R. Wördenweber *et al.*, Relaxor ferro- and paraelectricity in anisotropically strained SrTiO3 films. *J. Appl. Phys.* **113**, 164103 (2013).

26. E. D. Linnik *et al.*, Raman Response of Quantum Critical Ferroelectric Pb-Doped SrTiO3. *Crystals* **11**, 1469 (2021).

27. J. H. Haeni *et al.*, Room-temperature ferroelectricity in strained SrTiO3. *Nature* **430**, 758–761 (2004).

28. F. Eltes *et al.*, Low-Loss BaTiO $_3$ –Si Waveguides for Nonlinear Integrated Photonics. *ACS Photonics* **3**, 1698–1703 (2016).

29. Z. Ma *et al.*, Modeling of hysteresis loop and its applications in ferroelectric materials. *Ceram. Int.* **44**, 4338–4343 (2018).

30. H.-M. Christen *et al.*, Dielectric properties of sputtered SrTiO 3 films. *Phys. Rev. B* **49**, 12095–12104 (1994).

31. C. Weilenmann *et al.*, Single neuromorphic memristor closely emulates multiple synaptic mechanisms for energy efficient neural networks. *Nat. Commun.* **15**, 6898 (2024).

32. A. Riedhauser *et al.*, Absorption loss and Kerr nonlinearity in barium titanate waveguides. *APL Photonics* **10**, 016121 (2025).

33. T. Bearda *et al.*, "Overview of Wafer Contamination and Defectivity" in *Handbook of Silicon Wafer Cleaning Technology* (Elsevier, 2018; https://linkinghub.elsevier.com/retrieve/pii/B9780323510844000022), pp. 87–149.

34. A. Ulrich *et al.*, Raw data for "Engineering high Pockels coefficients in thin-film strontium titanate for cryogenic quantum electro-optic applications" publication, Zenodo (2025); https://doi.org/10.5281/ZENODO.16984395.

35. T. Hoshina *et al.*, Effect of oxygen vacancies on intrinsic dielectric permittivity of strontium titanate ceramics. *J. Ceram. Soc. Jpn.* **126**, 263–268 (2018).

36. Y. Luo *et al.*, Asymmetric Mach–Zehnder interferometer-based optical sensor with characteristics of both wavelength and temperature independence. *J. Opt.* **52**, 1008–1021 (2023).

37. C. Haffner *et al.*, All-plasmonic Mach–Zehnder modulator enabling optical high-speed communication at the microscale. *Nat. Photonics* **9**, 525–528 (2015).

38. G. Delhaye *et al.*, Structural properties of epitaxial SrTiO3 thin films grown by molecular beam epitaxy on Si(001). *J. Appl. Phys.* **100**, 124109 (2006).

39. J. O. Carneiro *et al.*, "Residual Stresses in Thin Films Evaluated by Different Experimental Techniques" in *Encyclopedia of Thermal Stresses*, R. B. Hetnarski, Ed. (Springer Netherlands, Dordrecht, 2014; http://link.springer.com/10.1007/978-94-007-2739-7_64), pp. 4222–4231.

40. D. A. Tenne *et al.*, Ferroelectricity in nonstoichiometric SrTiO3 films studied by ultraviolet Raman spectroscopy. *Appl. Phys. Lett.* **97**, 142901 (2010).

41. A. Gurung *et al.*, Modeling structure–properties relations in compositionally disordered relaxor dielectrics at the nanoscale. *J. Appl. Phys.* **134**, 104102 (2023).

42. K. S. Cole *et al.*, Dispersion and Absorption in Dielectrics II. Direct Current Characteristics. *J. Chem. Phys.* **10**, 98–105 (1942).

43. Y. P. Kalmykov *et al.*, Microscopic models for dielectric relaxation in disordered systems. *Phys. Rev. E* **70**, 041103 (2004).

44. M. Aellen *et al.*, Understanding Optical Gain: Which Confinement Factor is Correct? *ACS Photonics* **9**, 3498–3505 (2022).

45. Y. L. Li *et al.*, Phase transitions and domain structures in strained pseudocubic (100) Sr Ti O 3 thin films. *Phys. Rev. B* **73**, 184112 (2006).

46. R. Xu *et al.*, Strain-induced room-temperature ferroelectricity in SrTiO3 membranes. *Nat. Commun.* **11**, 3141 (2020).

47. D. Chelladurai *et al.*, Barium titanate and lithium niobate permittivity and Pockels coefficients from megahertz to sub-terahertz frequencies. *Nat. Mater.*, doi: 10.1038/s41563-025-02158-1 (2025).

48. T. Ostapchuk *et al.*, Soft-mode spectroscopy of BaTiO3 thin films. *J. Eur. Ceram. Soc.* **25**, 3063–3067 (2005).

49. J. Han *et al.*, Dielectric response of soft mode in ferroelectric SrTiO3. *Appl. Phys. Lett.* **90**, 031104 (2007).

50. G. Ghione, *Semiconductor Devices for High-Speed Optoelectronics* (Cambridge University Press, Cambridge ; New York, 2009).

51. R. A. De Souza, Oxygen Diffusion in $SrTiO_3$ and Related Perovskite Oxides. *Adv. Funct. Mater.* **25**, 6326–6342 (2015).

52. C. Kieninger *et al.*, Ultra-high electro-optic activity demonstrated in a silicon-organic hybrid modulator. *Optica* **5**, 739 (2018).

53. H. Xu *et al.*, Electro-Optic Activity in Excess of 1000 pm V^{-1} Achieved via Theory-Guided Organic Chromophore Design. *Adv. Mater.* **33**, 2104174 (2021).

54. C. Möhl *et al.*, Bidirectional microwave-optical conversion using an integrated barium-titanate transducer. arXiv arXiv:2501.09728 [Preprint] (2025). https://doi.org/10.48550/arXiv.2501.09728.

55. G.-W. Lu *et al.*, High-temperature-resistant silicon-polymer hybrid modulator operating at up to 200 Gbit s−1 for energy-efficient datacentres and harsh-environment applications. *Nat. Commun.* **11**, 4224 (2020).

Acknowledgments

We thank the electron beam lithography team for their expert assistance with sample fabrication, the RBS team for the characterization of our material, Sean McMitchell for the fruitful crystallographic discussions and Nathaniel Kinsey for providing valuable feedback.

Funding This research was funded by the Branco Weiss Society and the European Research Council (ERC) under the European Union’s Horizon 2020 research and innovation program:

ERC grant number 864483 NOTICE

ERC grant number 101042414 Q-AMP

Branco Weiss Fellowship

Author contributions

A.U. designed electro-optic and cutback structures, fabricated and measured electro-optic sample. K.B designed, fabricated and measured cryogenic to room-temperature RF devices. A.B epitaxially grew $SrTiO_3$, performed wafer characterization, fabricated optical cutback structures and performed room-temperature optical loss measurements. M.D. assisted cryogenic RF measurements. A.K. supported Piezoelectricity calculations and performed simulations. C.S assisted electro-optic measurements. Y.H helped with the electron-beam-lithography exposure of samples. S.S.S assisted wafer bonding flow in fabrication line. M.B supported epitaxial growth and performed RSM characterization and analysis. P.F performed TEM and EDS characterization and analysis. S.S and T.N. performed Raman characterization and analysis. K.V.G, B.K, K.D.G, C.M and C.H conceived and supervised the project. A.U., K.B., A.B., K.D.G and C.H. prepared the manuscript, with input from all authors.

Competing interests The authors declare no competing interests.

Data and materials availability All data needed to evaluate the conclusions in the paper are present in the paper and/or the Supplementary Materials. Datasets are available on Zenodo (*34*).

Supplementary Materials

Materials and Methods

Supplementary Text Sections 1 to 7,

Figs. S1 to S23,

Table S1,
References only called out in the Supplement Material *(35-55)*

Science
AAAS

Supplementary Materials for

Engineering high Pockels coefficients in thin-film strontium titanate for cryogenic quantum electro-optic applications

Anja Ulrich et al.

Corresponding author email: christian.haffner@imec.be

The PDF file includes:

Materials and Methods
Supplementary Text Sections 1 to 7
Figs. S1 to S23
Table S1

Materials and Methods

Growth

Heteroepitaxial $SrTiO_3$ thin films were grown on Si (001)-oriented substrates using MBE. The p-type Si (001) wafers were cleaned for 90 s in a 2% HF solution to remove part of the organic residues from the surface prior to introducing them to the ultra-high vacuum MBE growth chamber. To initiate the growth, the wafer was first heated, and a thin Sr layer was deposited to assist native oxide desorption. This led to a slight (3 x 2) surface reconstruction when the substrate was cooled down to 500°C. At this temperature the Sr interfacial layer was completed, achieving a ½ monolayer that forms an oxidation barrier between Si and $SrTiO_3$. This was confirmed by a (2 x 1) surface reconstruction on the RHEED pattern. After native oxide removal, direct epitaxy of the first 3 nm of $SrTiO_3$, with [100] $SrTiO_3$ (001) // [110] Si (001) (i.e. 45° rotation of the $SrTiO_3$ crystal with respect to Si) was performed in molecular oxygen at 350°C. After this, growth was paused to switch to atomic oxygen in the growth chamber and to increase the substrate temperature to 550°C. Under these conditions, the remaining $SrTiO_3$ epitaxy was completed at a growth rate of approximately 1 nm/min. Complementary information can be found in Supplementary 1.

Fabrication

Wafer Bonding Process: After growth, the wafer was annealed in oxygen at 850°C for 30 min to reduce the oxygen vacancy concentration in the $SrTiO_3$ layer caused by the reduced pressure environment during growth. Next, SiO_2 was deposited on top of $SrTiO_3$ by chemical vapor deposition (CVD) to enable subsequent wafer-to-wafer bonding with a SiO_2 on Si wafer. The top Si was then removed by grinding followed by a TMAH etch to end up with 105 nm $SrTiO_3$ on top of 2 μm SiO_2 on a Si substrate. Finally, an additional annealing in oxygen at 850°C for 30 min was performed.

Interdigitated finger capacitor (IDC) fabrication: Aluminum (Al) electrodes forming the interdigitated capacitors for RF measurements were patterned using a bilayer liftoff process. Photolithography was used to expose the resist and following the development 466 nm of Al was deposited using electron beam evaporation. After liftoff the devices were diced into small dies containing the different IDC geometries.

Electro-optic device: The process is illustrated in Fig. S1. Post wafer bonding, ~ 30 nm of chromium and ~ 140 nm of platinum were sputtered on the diced coupons using a bilayer liftoff process and electron beam lithography (EBL) for patterning. Following the liftoff, ~ 480 nm polymethyl methacrylate (PMMA) was spin coated while coupling gratings and waveguides with ~ 1.7 μm width were patterned using EBL. The meandered electrodes are roughly 15.37 mm long with a 10 μm electrode gap, 400 μm bending radius, 1.7 μm waveguide width and 200 μm unbalance in the two MZI arms [Supplementary 4.1].

RF measurement

Permittivity of thin-film $SrTiO_3$ was extracted by performing RF reflectometry analysis on interdigit finger capacitors (IDCs). An Attocube attoDRY800 closed cycle cryostat was used to lower the temperature of the IDCs to below 5 K. The capacitors formed by the interdigit electrodes, see Fig. S2 A, were electrically contacted using a GS probe at frequencies from 9 kHz to 14 GHz using a Keysight P5003B vector network analyzer (VNA). An excitation power of 0 dBm was applied, resulting in a probing field below 0.15 $\mathrm{V\mu m^{-1}}$. This small voltage can be considered a small signal perturbation with respect to the coercive field of $SrTiO_3$. The extraction of permittivity was limited to the range from 100 kHz to 1 GHz due to high-impedance behavior of the capacitor at low frequencies and the impact of resonances on the measurement at high frequencies. The aforementioned resonances are not material resonances; they arise from an increasing parasitic inductive impedance contribution at high frequencies, leading to series LC resonance behavior. Verification of the parasitic nature is obtained through changes to device geometry, which controllably reduce the capacitance and correspondingly shift the resonance position up (Fig. S3 B).

All RF permittivity measurements reported here are at 0 degrees assuming a multidomain (Fig. S13) mixed c- and a-axis structure in the thin-film plane, leading to an "effective" permittivity. A selection of IDC devices with varying finger lengths from 100 μm to 800 μm was used, the finger gap (w_{gap}) and width (w_{Finger}) were kept constant at 4 μm.

The impedance (Z), whose magnitude is seen in Fig. S3 A), was calculated based on the amplitude and phase of the reflected signal (S_{11}) via:

$$Z = 50\,\Omega \cdot \frac{1+S_{11}}{1-S_{11}}. \tag{1}$$

The phase of the impedance measurement showed a pure capacitive (-90°) behavior in Fig. S3 B. Thus, the impedance was mapped to a single total device capacitance (C) via:

$$\frac{1}{jZ\omega} = C. \tag{2}$$

We used COMSOL multiphysics simulation of the cross section in Fig. S2 B to match the measured capacitance to an effective permittivity of the $SrTiO_3$. Simulations show that SiO_2 and Si contributions can be neglected in C due to the very low permittivity, in strong contrast to that of $SrTiO_3$. To emphasize the negligibility of the SiO_2 (and implicitly the Si substrate) contribution we outline a first order estimation below. The parallel capacitance contribution of $SrTiO_3$ ($C_{\mathrm{SrTiO_3}}$) can be approximated by a parallel plate capacitor due to the large relative permittivity (ε_r) where $h_{\mathrm{SrTiO_3}}$ is the height of the $SrTiO_3$ layer and $\#_{Fingers}$ is the number of IDC fingers:

$$C_{\mathrm{SrTiO_3}} = \varepsilon_{\mathrm{r,SrTiO_3}} \cdot \varepsilon_0 \cdot \frac{\left(L\cdot\#_{\mathrm{Fingers}}\cdot h_{\mathrm{SrTiO_3}}\right)}{w_{\mathrm{gap}}}. \tag{3}$$

Similarly, the perpendicular SiO_2 capacitance ($C_{\mathrm{SiO_2}}$) can also be approximated by a parallel plate capacitor:

$$C_{\mathrm{SiO_2}} = \varepsilon_{\mathrm{r,Si}} \cdot \varepsilon_0 \cdot \frac{w_{\mathrm{Finger}} \cdot L \cdot \#_{\mathrm{Fingers}}}{h_{SiO2}}. \tag{4}$$

For the given geometry their ratio is:

$$\frac{C_{\mathrm{SrTiO_3}}}{C_{\mathrm{SiO_2}}} = \frac{\varepsilon_{\mathrm{r,SrTiO_3}}}{\varepsilon_{\mathrm{r,Si}}} \cdot \frac{h_{\mathrm{SrTiO_3}} \cdot h_{\mathrm{SiO_2}}}{w_{\mathrm{gap}} \cdot w_{\mathrm{Finger}}} \approx \frac{\varepsilon_{\mathrm{r,SrTiO_3}}}{\varepsilon_{\mathrm{r,Si}}} \cdot \frac{1}{100}. \tag{5}$$

Consequently, the thin-film capacitance contributes approximately 10 times more than the buried oxide capacitance. In the above arguments it was shown that the measured device capacitance is dominated by the $SrTiO_3$ layer.

The frequency-dependent permittivity response indicates there are no significant material resonances within the measured range. Such material resonance contributions would result in a significantly reduced permittivity at higher frequency and thus limit the electro-optic bandwidth potential of $SrTiO_3$. The primary transverse optical phonon mode (TO_1) of the Slater mode, responsible for the high permittivity of $SrTiO_3$, is only expected to occur as high as 2.75 THz (*35*). Therefore, the possibility for even higher operating bandwidths before encountering large losses due to intrinsic (material) limitations associated with the TO_1 phononic mode exists. Moreover, extrinsic loss mechanisms arising from material defects are expected to play a more dominant role in this respect.

MZI time domain signal & Pockels coefficient extraction

The electrically modulated time signal of the optical power is governed by the MZI‘s transfer function. In our design the grating couplers are too close to the splitter and higher order modes leaking to the splitter resulted in a limited extinction ratio due to asymmetric power splitting. For an asymmetric splitting ratio k the MZI transfer function is given by (*36*):

$$P(t) \propto |E_{out}|^2 = P_0\left((1-k)^2 + k^2 + 2k(1-k)\cos\left(\tfrac{2\pi}{\lambda}\cdot \mathit{\Delta} n_{\mathrm{eff}}\cdot L + \theta\right)\right). \tag{6}$$

Here θ corresponds to the MZI's zero voltage operation point and is given by the 200 µm unbalance of the two MZI arms and the laser wavelength λ. L is the electrode length and $\mathit{\Delta} n_{\mathrm{eff}}$ is the voltage induced effective refractive index difference [Supplementary 4.2]. The splitting ratio (k) was extracted from the time signal by solving:

$$\frac{P_{\mathrm{min}}}{P_{\mathrm{max}}} = 1 - 4k + 4k^2. \tag{7}$$

The optical power can be transformed to a phase via:

$$\Delta\Psi(t) = \cos^{-1}\left(\frac{\left(\frac{P(t)}{P_0} - (1-k)^2 - k^2\right)}{2k(1-k)}\right) = \theta + \frac{2\pi}{\lambda}\cdot \mathit{\Delta} n_{\mathrm{eff}}\cdot L, \tag{8}$$

resulting in Fig. S4. The phase depicted is wrapped by the arccosine function and needs to be unwrapped for every turning maximum/minimum. Normally, the phase should oscillate between 0 and π, however, the 10 kHz bandwidth of the photodiode in combination with the strong overmodulation (~ 40π phase change) caused a low-pass behavior that prevents the full oscillations from 0 to π. The low-pass characteristic was compensated in the post processing, by manually extending the turning points to 0 or π as shown in Fig. S5 A.

After unwrapping (Fig. S5 B) and subtraction of the operation point, θ results in a continuous phase change curve vs applied field, as shown in the main text.

The change in effective refractive index can then be extracted using (*37*):

$$\mathit{\Delta} n_{\mathrm{eff}} = \mathit{\Gamma}\cdot\frac{\mathit{\Delta} n_{\mathrm{mat}}}{n_0}\cdot n_{\mathrm{g}} = \mathit{\Gamma}\cdot\left(-\frac{1}{2}\cdot n_0^2\right)\cdot\left(r(\varepsilon_{\mathrm{r}})\cdot v(\varepsilon_{\mathrm{r}})\cdot E_{\mathrm{AC}} + R(\varepsilon_{\mathrm{r}})\cdot E_{\mathrm{AC}}^2\right)\cdot n_{\mathrm{g}}, \tag{9}$$

where E_{AC} is the electric field induced by the applied sinusoidal voltage. r_{eff} can then be extracted from the derivative of the effective refractive index change ($r_{\mathrm{eff}} \propto \frac{d\Delta n_{\mathrm{eff}}}{dE_{\mathrm{AC}}}$). However, the little peaks in the zoom in Fig. S5 B below, arising from the manual extension of the turning points, leads to medium-sized peaks on top of the Pockels coefficient poling curve's envelope due to the numerical implementation of the derivative. For a detailed derivation of the Pockels extraction, see Supplementary 4.2.

Supplementary Text

Supplementary 1 Growth

The quality of the epitaxial layer is key for implementing $SrTiO_3$ as an active material in quantum applications. In our previous work, we demonstrated the critical role of stoichiometry and $SrTiO_3$ thickness on the structural, optical and electrical properties (*21*). $SrTiO_3$ films which are slightly off in stoichiometry still resulted in a good crystalline quality, which is essential for the film in this work (Sr/Ti = 0.96 ± 0.03). Fig. S6 shows the dependence of cationic stoichiometry (Sr/Ti) and $SrTiO_3$ (002) ω-scan FWHM on the effective permittivity ε_r at cryogenic temperatures for four different $SrTiO_3$ films. In a ω-scan, the XRD detector is fixed at an unchanging angle while the sample is tilted slightly. To maximize the permittivity, achieving a minimal FWHM is crucial, which can be attained by approaching ideal stoichiometry and increasing the $SrTiO_3$ thickness.

Supplementary 2 Theoretical thermal strain calculations at 4 K

Besides the ferroelectric behavior of our $SrTiO_3$ due to stoichiometry, strain can also elevate T_C and contribute to a ferroelectric phase transition at cryogenic temperatures. This dependency can be seen on the phase diagram in Fig. S7, which illustrates the behavior of T_C as a function of in-plane strain (*27*). Room-temperature reciprocal space mapping (RSM) indicates a fully relaxed $SrTiO_3$ layer with unit cell equal to bulk, see Fig. S8. The relaxation in epitaxial films can be facilitated by dislocation gliding during thermal treatment. Nevertheless, strain can be induced at cryogenic temperatures due to the difference in thermal expansion coefficients (CTE) between film and substrate ($CTE_{SrTiO3} = 8.8 \cdot 10^{-6}\ K^{-1}$, $CTE_{Si} = 2.6 \cdot 10^{-6}\ K^{-1}$) (*38*). Due to this mismatch, silicon contracts slower than $SrTiO_3$ upon cooling. Because the Si substrate (725 µm) is much thicker than the SiO_2 layer (2 µm), the SiO_2 layer, and consequently the $SrTiO_3$ film, will contract following the Si substrate upon cooling. Even though the film is not epitaxially attached to the silicon, it is still mechanically bonded to the SiO_2 layer. Because of thickness and stiffness, the thermal behavior of Si dominates and gets transmitted to the $SrTiO_3$ layer. Assuming our $SrTiO_3$ film to be isotropic, the induced biaxial thermal strain can be calculated by (*39*):

$$Strain_{\mathrm{thermal,SrTiO_3}} = \left(CTE_{\mathrm{SrTiO_3}} - CTE_{\mathrm{Si}}\right) \cdot \Delta T\ . \tag{10}$$

At 4 K this results in a tensile strain of 0.18%, which would be the upper limit of the induced strain at cryogenic temperatures for our sample. 0.18% strain (blue cross) corresponds to 50 K < T_C < 110 K (Fig. S7), aligning with the permittivity measurements and reported T_C in the main text.

Supplementary 3 Relaxor ferroelectricity

Temperature-dependent Raman spectroscopy shows the gradual appearance of the Slater and Last phononic mode at 5.2 THz upon cooling. Fig. S9 B illustrates the fitted peak intensity by an asymmetric profile as a function of temperature. The peak at 5.2 THz starts to appear below 200 K. The precise temperature of this phonon modes' appearance is independent of whether the sample is cooled down (blue) or warmed up (red). The presence of the Raman signal is a clear indicator of ferroelectricity, as this mode is only Raman active under non-centrosymmetric structure conditions. Literature links the gradual appearance of this signal to the relaxor behavior coming from polar nanoregions (*24*, *26*, *40*).

As a generalization of the Debye relaxation model either the Cole-Cole model or the Havriliak-Negami model (more flexible) can be used for describing the phenomenon of relaxor ferroelectricity. They include a broadening parameter α for the relaxation time τ, and the Havriliak-Negami model introduces another shape parameter β for asymmetric broadening. This extra parameter reflects a non-uniform distribution of relaxation times, often due to structural disorder, interfacial effects or local heterogeneities such as polar nanoregions (*41*).

Cole-Cole model (*42*):

$$\varepsilon^*(\omega) = \varepsilon_\infty + \frac{\varepsilon_s - \varepsilon_\infty}{1 + (i\omega\tau)^{1-\alpha}} \tag{11}$$

Havriliak-Negami model (*43*):

$$\varepsilon^*(\omega) = \varepsilon_\infty + \frac{\varepsilon_s - \varepsilon_\infty}{(1 + (i\omega\tau)^{1-\alpha})^{\beta}} \tag{12}$$

The fitting results (Fig. S10) show almost no differences between both models ($\beta = 0.98 \pm 0.1$). This indicates good crystallinity of the film and rather small polar nanoregions, confirming our material characterization results. Because of this, here we only show the fitting of the Cole-Cole model. Following the model, the corresponding relative permittivity at 1 GHz will be ~ 2400.

Fitting parameters Cole-Cole model:

- Static permittivity ε_s: 3085 ± 80
- High-frequency permittivity ε_∞: 2069 ± 70
- Relaxation time τ: $6.2 \times 10^{-9} \pm 1.7 \times 10^{-9}$ s
- Broadening parameter α: 0.82 ± 0.03

Supplementary 4 Electro-optic measurements

Supplementary 4.1 Setup & Device

The MZI device is cooled down below 5 K with the same cryostat as the RF setup. However, in and outcoupling via two fibers required us to remove the RF probe shown in Fig. S11 A. The sample is silver pasted onto the sample holder and the gratings of the sample are interfaced using angled fibers on piezo stages, which can be controlled individually to change the grating coupling efficiency. A tunable Keysight N7778C laser at around 1470 nm is used to send in an optical signal. The electrodes are wirebonded with Al wires to a PCB which is connected to either the Keysight 33512B arbitrary waveform generator (AWG) or the Keysight B2910BL precision source measure unit (SMU). The former can supply up to 20 MHz and 10 V peak sinusoidal drive signal while the latter one can be programmed to output a sinusoidal signal up to 1 kHz with up to 40 V peak voltage. The electrically modulated optical signal at the optical output is detected using a Keysight N7744C photodetector (PD) which has a 10 kHz 3 dB cutoff frequency.

The sample holder limits the sample size to below 1 cm^2, as shown in Fig. S11 A. Therefore, meandered electrodes have been used instead of straight ones to increase the interaction length and the modulated output signal. The electrodes are roughly 15.37 mm long with a 10 µm electrode gap, 400 µm bending radius, 1.7 µm waveguide width and 200 µm unbalance in the two MZI arms.

Supplementary 4.2 Effective Pockels coefficient extraction

From equation (8) the change in refractive index is related to the phase change via:

$$\Delta n_{\text{eff}} = \Delta\Psi \cdot \frac{\lambda}{2\pi \cdot L} - \theta\,. \tag{13}$$

It can also be defined as (*37*):

$$\mathit{\Delta} n_{\text{eff}} = \mathit{\Gamma} \cdot \frac{\mathit{\Delta} n_{\text{mat}}}{n_0} \cdot n_{\text{g}} = \mathit{\Gamma} \cdot \left(-\frac{1}{2} \cdot n_0^2\right) \cdot \left(r(\varepsilon_{\text{r}}) \cdot v(\varepsilon_{\text{r}}) \cdot E_{\text{AC}} + R(\varepsilon_{\text{r}}) \cdot E_{\text{AC}}^2\right) \cdot n_{\text{g}}, \tag{14}$$

E_{AC} is the electric field induced by the applied sinusoidal voltage. The data shown in the main figure were obtained by a 20 Hz and 16 V amplitude dropping over 10 µm electrode spacing. The change of refractive index of the optical mode is determined by the material's refractive index change coming from the linear electro-optic Pockels coefficient r_{eff} and quadratic electro-optic Kerr coefficient R. This change scales with the light confinement in the $SrTiO_3$ (Γ), the poling fraction v and with the group refractive index n_{g}. With the above definition $\mathit{\Gamma}$ corresponds to the energy confinement factor which is (*44*):

$$\Gamma = \frac{\int_{A_{\text{SrTiO}_3}} \varepsilon_r |\boldsymbol{E}|^2 dA}{\int_A \varepsilon_r |\boldsymbol{E}|^2 dA} = 43\%, \tag{15}$$

where the numerator expression is integrated over the $SrTiO_3$ area and the denominator over the overall area of the optical mode. The poling function v is given by (*29*):

$$v = \frac{\sinh(U \cdot (E \pm E_{\text{C}}))}{U/\chi - 1 + \cosh\left(U \cdot (\mathrm{E} \pm E_{\text{C}})\right)}, \tag{16}$$

where U is the equivalent field, E_{C} the coercive field and the linear electric susceptibility $\chi = \varepsilon_{\text{r}} - 1$.

From the unwrapped phase and equation (14) r_{eff} can be extracted by taking the derivative with respect to the applied electric field:

$$\begin{aligned} r_{\text{eff}} &= \frac{d\Delta n_{\text{eff}}}{dE_{\text{AC}}} \cdot \frac{2}{\Gamma \cdot n_{\text{g}} \cdot n_0^2} = \frac{d\Delta\Psi}{dE_{\text{AC}}} \cdot \frac{2\lambda}{2\pi \cdot L \cdot \Gamma \cdot n_{\text{g}} \cdot n_0^2} \\ &= \left(r(\varepsilon_{\text{r}}) \cdot \frac{dv}{dE_{\text{AC}}} \cdot E_{\text{AC}} + r(\varepsilon_{\text{r}}) \cdot v(\varepsilon_{\text{r}}) + 2R(\varepsilon_{\text{r}}) \cdot E_{AC}\right) \cdot \end{aligned} \tag{17}$$

For most ferroelectric materials the linear Pockels coefficient r will dominate over the quadratic Pockels coefficient and R can be neglected. In the case where we are fully poled $\frac{dv}{dE_{\text{AC}}} = 0$ and $v \approx 1$ such that we are left with $r_{\text{eff}} \approx r(\varepsilon_{\text{r}})$. The derivative of the phase is shown in Fig. S12 A. The red curve shows a nonlinear decaying trend for negative voltages in the downwards sweep direction and similarly for the blue curve in the positive voltage upward sweep direction. Instead, the curve should flatten out as one would expect from the fully poled case with poling function being equal to one as seen in Fig. S12 B or a linear decay due to a strong Kerr coefficient as seen in Fig. S12 C. It was not possible to find a good physical fit using equation (17). The origin of the previously mentioned decays is attributed to the Pockels coefficients direct relation to the permittivity $r(\varepsilon_{\text{r}})$,which falls with increasing bias magnitude (*25*). This dependence is not included in equation (17) and requires further investigations.

Due to space constraints of the setup the Pockels value given by equation (17) needs to be corrected for the effective contribution of different crystal directions along the waveguide arising from the meandered layout.

According to theoretical studies (*45*, *46*), perturbated $SrTiO_3$ is predicted to be in a 4mm or mm2 point group, the former being the point group of $BaTiO_3$. Both point groups have the off-diagonal r_{51} element in plane for an a-axis dominated film. For complex oxides like $BaTiO_3$ the permittivity is typically lower for the c-axis due to a stronger confinement of the Ti atom in the ferroelectric potential wells, which leads to a reduced polarizability. Therefore, it can be expected that the r_{33} and r_{13} coefficients with the RF field along the c-axis of the crystal are lower compared to r_{51} with the RF field along the a-axis (Miller's rule).

Preliminary measurement along the r_{33} direction confirm a reduced Pockels strength compared to the 45° case. Thus, in the following we neglect the r_{33} contribution and can define the effective Pockels coefficient as (*47*):

$$r_{\mathrm{eff}}(\theta) = \sum_{\varphi} \sigma_{\varphi} \cdot \left(\cos^2(\theta) \cdot \sin(\theta) \ \cdot (r_{13} + 2r_{51})\right), \tag{18}$$

where θ is the device angle with respect to the z-axis and crystalline domains (Fig. S13 A & B). The domain direction in Fig. S13 A is given by ϕ equal to $0°, 90°, 180°$ or $270°$ and corresponds to the optical propagation direction θ where the RF field points along the domains. Applying a bias significantly stronger than the coercive field will result in flipping of domains (Fig. S13 C) and $\upsilon = \pm 1$. The light travelling in direction θ with the RF and optical polarization (TE mode) perpendicular to θ experiences different domains orientations. This is reflected in the sum sign and the averaging factor σ_{φ} in equation (18) with condition $\sum_{\varphi} \sigma_{\varphi} = 1$. For the simplified fully poled case there will be only two contributing domain directions, i.e. $\sigma_{\varphi} = 0.5$, namely $\theta + 0°$ and $\theta + 90°$ and equation (18) can be rewritten to:

$$r_{\mathrm{eff}}(\theta) = 0.5 \cdot \left((\cos\theta \sin^2\theta + \sin\theta \cos^2\theta) \cdot \mathrm{sgn}(\upsilon_{\varphi}) \cdot (r_{13} + 2r_{51}) \right). \tag{19}$$

Here the $\cos\theta$ term maps onto the $\theta + 90°$ crystal domain and the $\sin\theta$ term maps onto the $\theta + 0°$ domain. In the equation we included the $\mathrm{sgn}(\upsilon_{\varphi})$ of the poling function as we propagate along different directions, with the poling function being either plus or minus one, in our device. We use the same definition as for the electric field mapping, i.e. the $\phi = 0°, 90°$ domains have a positive poling polarity and the $\phi = 180°, 270°$ a negative poling polarity.
For the straight parts of our design θ equals 45°, 225° or 135° (Fig. S14), which equals $|\cos\theta \sin^2\theta\,| + |\sin\theta \cos^2\theta| = 1/(\sqrt{2})$ for all directions and involves two domains which determine the sign. Neglecting the electrode bends, we can write the effective measured Pockels coefficient of our device as:

$$r_{\mathrm{eff,meas}} = 0.22 \cdot r_{\mathrm{eff}}(\theta = +45°) + 0.23 \cdot r_{\mathrm{eff}}(\theta = +225°) + 0.08 \cdot r_{\mathrm{eff}}(\theta = 135°), \tag{20}$$

where the straight parts have been scaled by the percentage of overall length in this direction. I.e. for 22% of the electrode length light travels in the 45° direction, where the fully poled 0° and 90° domain are experienced equally strong ($\sigma_{\varphi} = 0.5$), both contributing a factor $1/(2\sqrt{2})$ with a positive polarity. Therefore, $r_{\mathrm{eff}}(\theta = +45°) = 0.5 \cdot \left(2 \cdot 1/(2\sqrt{2})\right) \cdot (r_{13} + 2r_{51}) = 1/(2\sqrt{2}) \cdot (r_{13} + 2r_{51})$. The expressions of the other directions can be found in Table S1.
The same needs to be done for the bends ($\sim 2.5 \cdot 2\pi$) contributing 47% to the overall length. Here we assumed the simplified full poled case as well, which overestimates the bend contribution. Due to symmetry, it is sufficient to calculate the integral for a quarter circle. This gives:

$$r_{\text{eff,quarter bend}} = \frac{1}{\frac{\pi}{2}} \cdot \left(\int_0^{\frac{\pi}{2}} \frac{1}{2} \cdot \ (\cos\theta \sin^2\theta + \sin\theta \cos^2\theta) d\theta \cdot (r_{13} + 2r_{51}) \right) \\ = \frac{1}{\pi} \cdot \frac{2}{3} \cdot (r_{13} + 2r_{51}). \tag{21}$$

Thus equation (20) becomes:

$$r_{\text{eff,meas}} = 0.22 \cdot r_{\text{eff}}(\theta = +45°) + 0.23 \cdot r_{\text{eff}}(\theta = +225°) \\ +0.08 \cdot r_{\text{eff}}(\theta = 135°) + 0.47 \cdot r_{\text{eff,quarter bend}}. \tag{22}$$

Using the calculated expression in Table S1 and equation (21) yields:

$$r_{\text{eff,meas}} = \frac{(r_{13} + 2r_{51})}{2\sqrt{2}} \cdot \left(0.22 + 0.23 + 0.08 + 0.47 \cdot \frac{2}{3\pi} \cdot 2\sqrt{2}\right) \approx 0.81 \cdot r_{\text{eff}}. \tag{23}$$

The compensated effective value reported in the main text for 20 Hz is:

$$r_{\text{eff}} = \frac{(r_{13} + 2r_{51})}{2\sqrt{2}} = \frac{r_{\text{eff,meas}}}{0.81} \approx 345 \text{ pm/V}, \tag{24}$$

here $r_{\text{eff,meas}} \propto \Delta n_{\text{eff}}/L \approx 280 \text{ pm/V}$ corresponds to the experimentally extracted phase shift (equation (9)) divided by the full length, not accounting for the correction from different directions. By solving equation (9) for a π phase shift the half-wave-voltage length product $V_\pi L$ can be calculated:

$$V_\pi L \approx E_{AC} \cdot d \cdot L = \frac{\lambda_0 \cdot d}{\Gamma \cdot n_0^2 \cdot n_{\text{g}} \cdot r_{\text{eff}}} \approx 1.04 \pm 0.08 \text{ Vcm}, \tag{25}$$

where $d = 10$ µm is the electrode distance.

Using $r_{\text{eff}} \approx 345 \text{ pm/V}$ and the zero-bias voltage permittivity $\varepsilon_{\text{r}} \approx 2700$ we can estimate our Miller's coefficient (*6*):

$$\delta_{\text{M2}} = \frac{r_{\text{eff}} \cdot n_0^4}{2(\varepsilon_{\text{r}} - 1) \cdot (n_0^2 - 1)^2} \approx 0.1 \cdot 10^{-12} \frac{\text{m}}{\text{V}}. \tag{26}$$

Supplementary 4.3 Small signal modulation

To verify the AC poling from the chapter before, a strong but slowly varying sinusoidal signal (20 Hz, 1.6 µm/V) combined with a weak and fast varying sinusoidal signal (1 kHz, 0.05 V/µm) , close to the limit of our photodetector, was applied as shown in Fig. S15 A. Therefore equation (8) is changed to:

$$\Psi(t) = \cos^{-1}\left(\frac{\left(\frac{P(t)}{P_0} - (1-k)^2 - k^2\right)}{2k(1-k)} \right) = \theta + \frac{2\pi}{\lambda} \cdot (\Delta n_{\text{eff,20Hz}} + \Delta n_{\text{eff,1kHz}}) \cdot L \tag{27}$$

containing both frequency contributions. To extract the contribution from the 1 kHz signal the maxima and minima of the drive signal without the fast signal can be used for overlapping as shown in Fig. S15 B). The subtraction of the 20 kHz contribution can then be fitted and yields $r_{\text{eff,1kHz}} \approx 134 \pm 2 \text{ pm/V}$. This confirms the value obtained from the poling curve in the main text for maximal poling field of 1.6 V/µm and relies on the bandwidth of r_{eff} being constant up to 1 kHz.

Supplementary 4.4 Bandwidth

Due to the low optical output power of - 50 dBm of our device and the limited bandwidth of the used PD, the time signal cannot be resolved anymore for frequencies beyond 1 kHz. Therefore, a time averaging method was used to measure the electro-optic frequency response beyond 1 kHz. As shown in the inset in Fig. S16 A, the laser is set to a constructive interference point (”on”-point) of the MZI and a weak ac signal of 0.1 V/µm is applied to minimize the effect of any third-order nonlinear and poling contributions. The time averaged power at the PD is reduced due to the symmetric oscillations around the on-point with an averaging time $t_{\mathrm{avg}} \gg 1/f_{\mathrm{AC}}$:

$$P_{\mathrm{on}} - \mathrm{P(t)} = P_{\mathrm{on}} - \frac{P_{\mathrm{on}}}{t_{\mathrm{avg}}} \int_0^{t_{\mathrm{avg}}} \left(\frac{1}{2} + \frac{1}{2} \cdot \cos\left(\frac{2\pi}{\lambda} \cdot \Delta n_{\mathrm{eff}}(t) \cdot L \right) \right) dt \geq 0. \tag{28}$$

The reduction is directly proportional to the strength of the effective Pockels coefficient at the different frequencies as given by equation (28) with $\Delta n_{\mathrm{eff}} \propto r_{\mathrm{eff}} \cdot \upsilon \cdot E_{\mathrm{AC}}(t)$. The optical power difference is unaffected by an increase in ac modulation frequency, indicating a constant effective Pockels coefficient up to 1 MHz. The bandwidth curve in Fig. S16 A shows a resonance at 5 MHz (vertical dashed line). The source of the 5 MHz resonance was identified by characterizing the low frequency lines without a sample connected. An S11 reflection measurement (Fig. S16 B) shows that the system (without sample) has resonances appearing from 1 MHz onwards; therefore, limiting higher speed measurements and clarifying the origin of the resonance seen in our bandwidth data. The reduced response time for frequencies below 50 Hz, preventing DC bias experiments, is believed to be due to screening [Supplementary 4.5].

In addition to the time-averaged method presented in Fig. 3 F, we performed sideband modulation experiments to confirm that the modulation is driven by a Pockels effect (i.e. Stokes and anti-Stokes generation). We applied a small-signal (E = 0.2 V/µm < E_c) sinusoidal ac modulation up to 10 MHz. For that we tracked the power in the sideband via connecting an electrical spectrum analyser (ESA, Keysight N9000B, 9Khz to 14 GHz) to a photodiode (PD, FPD610, MenloSystems 500 MHz bandwidth). Fig. S17 A shows the 1st sideband power for different applied voltages, following the trend $P_1 \propto E^2$ that is expected from a Pockels effect. The resonance peak around a few MHz is attributed to the low-frequency behaviour of the DC lines (see Fig. S16). Furthermore, we performed optical power measurements in time up to 9 kHz modulation frequency, like Supplementary 4.6. Using equation (8) the phase change was extracted. The result is depicted in Fig. S17 B. The drive voltage was chosen deliberately low such that no poling occurs as the standard MZI model used does not account for this. As mentioned in Supplementary 4.1 our power meter has a cutoff around 10 kHz which can be clearly seen. Frequencies below 10 Hz show a reduced phase change, which we link to a reduced response due to low frequency screening [Supplementary 4.5]. As the ESA is limited to 9 kHz and our optical power meter to around 10kHz, the time averaging modulation efficiency measurements covers the widest frequency range from 10Hz to 10MHz as shown in Fig. 3 F) and overlapping with our ac poling data.

In the following the implications of this work for the performance of an electro-optic modulator are further elaborated.

The bandwidth of an electro-optic modulator is fundamentally constrained by three main factors. First, intrinsic material limitations arise from the phononic origin of the Pockels effect. In materials like Barium Titanate ($BaTiO_3$), the high electro-optic response is driven by soft phonon modes, particularly the overdamped component of the transverse optical (TO_1) mode. At room temperature, this mode is associated with a high dielectric permittivity due to its low frequency, typically around 40 cm^{-1} (~ 1.2 THz) (*48*). This sets a theoretical upper bound for the modulation bandwidth, as the electro-optic response diminishes beyond the phonon resonance. Bulk $SrTiO_3$ features a high-permittivity phononic mode of similar frequency (*49*), this in combination with a larger T_C for our thin-film should indicate a similar high intrinsic material bandwidth. Second, in a traveling-wave MZI modulators, bandwidth is limited by three factors: velocity mismatch (walk-off) between the RF and optical signal, impedance mismatching and RF losses (*50*). The bandwidth of such a device, assuming impedance matching and negligible RF losses will be dominated by the group mismatch between the optical carrier and RF drive ($\Delta n = \sqrt{\varepsilon_{\mathrm{eff,RF}}} - n_{\mathrm{g,opt}}$). The cutoff frequency is then given by (*50*):

$$f_{3\mathrm{dB}} \approx \frac{1.89 c_0}{\pi L(\sqrt{\varepsilon_{\mathrm{eff}}} - n_{\mathrm{g,opt}})} \tag{29}$$

where c_0 is the speed of light, L is the device length, $\varepsilon_{\mathrm{eff}}$ is the RF refractive index and $n_{\mathrm{g,opt}}$ the optical group refractive index. This frequency is limited by the minimal device length. Common configurations are based on SiN loaded waveguides that enable a reduction of the electrode spacing to 6µm with metallic losses << 1 dB/cm, resulting in a $V_\pi L$ of 0.35 Vcm. Assuming push-pull and typical drive voltages of 2-3 V, devices can be as short as 1 mm. Assuming a device length of 1 mm, an RF effective permittivity (refractive index) of approximately 20 (≈ 4.47) to 30 (≈ 5.48), and an group optical index of approximately 2.13, the cutoff frequency ranges from approximately ~53 GHz to ~77 GHz, depending on the RF permittivity.

Finally, in lumped-element configurations, as used in a resonator, electro-optical bandwidth limitation will be governed by the RC time constant. For a 100 µm long device with a 6 µm electrode spacing we numerically calculated device capacitance of 0.8 fF/µm. This in combination with a 50 Ω source resistance results in a 3 dB bandwidth of

$$f_{3\mathrm{dB}} = \frac{1}{2\pi \cdot 8\mathrm{fF} \cdot 50\Omega} = 40\ \mathrm{GHz}$$

Depending on the application (e.g. electro-optical transducers) bandwidth can be further limited by the optical and/or electrical cavity bandwidth limitations. The above discussion has been added to the supplement material.

Supplementary 4.5 DC screening

Applying a DC bias to the electrodes initially induces a change in the optical output signal. However, this is followed by a several second long decay of the optical power towards the no-bias baseline of the MZI. This screening behaviour is shown in Fig. S18 A for different bias voltages. The measurement indicates a faster decay for higher voltages.

For memristors it is shown that bulk $SrTiO_3$ with the same metals as in our device can create or absorb oxygen vacancies depending which voltage polarity is applied (*31*). These vacancies could build up an internal screening field as shown in Fig. S18 B which could lead to a net electric field of zero within the nonlinear material and therefore to a vanishing effective Pockels coefficient. As the room temperature diffusion coefficient of oxygen vacancies D ≈ 1e-14 cm^2/s (*51*) is low and should be even lower for cryogenic temperatures, a diffusion of generated vacancies across the electrode gap of 10 µm can be excluded.

The TEM and energy-dispersive X-ray spectroscopy (EDS) results of the device at two different positions are shown in Fig. S19 A. The EDS under the electrodes in Fig. S19 B shows a gradient in oxygen, titanium and strontium as well as oxidization of the chromium interface layer while

Fig. S19 C shows a constant oxygen concentration through the $SrTiO_3$ film. The gradient could originate from the $SrTiO_3$ reduction by chromium.

Supplementary 4.6 Room-temperature Measurements

Fig. S20 shows the optical output power versus three ac modulation periods at room temperature for a 200 Hz drive signal with an ac amplitude of 1 µm/V. The optical output power shows double the applied modulation frequency which is a clear indicator for a quadratic electro-optic Kerr effect; no Pockels effect is evident. The output signal can be fitted using equation (6) yielding a quadratic electro-optic Kerr coefficient of $R \approx 4.4 \cdot 10^{-18} \pm 1.3 \cdot 10^{-20}\ \mathrm{m^2/V^2}$.

Supplementary 5 Effective Pockels Coefficient Data

The material induced change in refractive index is given by equation (14) ($\Delta n_{\mathrm{mat}} \propto (n_0^3 \cdot r_{\mathrm{eff}})$. To disentangle design and device performances from the actual nonlinearity of different materials (see Γ and n_{g} in equation (14)) $n_0^3 \cdot r_{\mathrm{eff}}$ is chosen as the figure of merit to compare different materials with each other. For completeness $\alpha V_\pi L$ of our device is 5.72 VdB which is larger, but further optimization of losses should be possible.

In the following we provide background information on the extraction procedure of the stated Pockels coefficients shown in Fig. 1 A in the main text. We provide motivation and the selection of references.

OEO: We are aware that certain OEO materials like pure, "bulk" JRD1 feature an electro-optic strength $n^3 \cdot r$ up to 2300 pm/V (*52*) or even 9000 pm/V for BAY1 (at 1310 nm) (*53*). This is a larger value than the one indicated in the main text. However, these high Pockels coefficient in these materials go hand in hand with increased optical losses (*53*) which are undesired for quantum applications. Therefore, to make a more appropriate comparison, OEO materials featuring the lowest losses have been considered. These are also the materials that have been used by the community for cryogenic operation. The Pockels coefficient of OEO is driven by hyperpolarizability and not permittivity. As the main contribution to the permittivity is of electronic nature, only a small reduction in Pockels coefficient is expected when cooling down.

$LiNbO_3$: Bulk $LiNbO_3$ can be grown on wafer scale using different growth techniques such as the Czochralski method (*10*). This combined with the development of the "smart cut" technology – ion slicing of bulk crystal and post wafer bonding onto an insulating substrate - enabled high-quality thin films.

$BaTiO_3$: Reference (*8*) reports Pockels values of $r_{\mathrm{eff}} \approx 170$ pm/V corresponding to a third of its room temperature value $r_{\mathrm{eff}} \approx 520$ pm/V. Highest Pockels values are achieved for full poling of the thin film. For this, the bias field needs to be above the coercive field of 8 V/µm (4 K), 0.5 V/µm (300 K). The reported permittivity values for different bias fields converge to a value of around 100-150 for 4 K. This corresponds to a reduction of roughly 84-90% compared to the room-temperature permittivity of 925 for the unbiased case (no bias data given for biases in between 0 and 4.8 V/µm). Following Miller's empirical rule, a cryogenic Pockels value of $r_{\mathrm{eff}} \approx 57$ to 85 pm/V is expected. Recently, values of 13 pm/V at mK have been reported (*54*).

Supplementary 6 Optical losses

Optical losses of the material are a crucial parameter for quantum applications. Fig. S21 shows the material losses of various Pockels materials. Cryogenic material losses of these materials has not yet been clearly reported which is why only room temperature values are compared here. The ferroelectric complex oxides have a bandgap of around 3-4 eV while the organic chromophores have a bandgap of around 1.5 eV in the visible. Thus, OEO commonly have a strong absorption peak around 850 nm wavelengths (*15*), which physically limits their material losses at 1550 nm in the telecommunication regime.

The material losses of 5.5 dB/cm in this work can be seen as an upper limit as it attributes the full propagation losses exclusively to the $SrTiO_3$, not considering other loss channels such as PMMA material or scattering losses [Supplementary 7]. Compared to $LiNbO_3$ with 0.2 dB/m, OEO with 3 dB/cm and $BaTiO_3$ with 0.2 dB/cm, our material is situated at the upper end in Fig. S21.

Further loss reduction efforts of our thin-film $SrTiO_3$ is needed to approach loss values observed in $BaTiO_3$ and bulk $SrTiO_3$ values of below 0.2 dB/cm (*20*).

In the following we provide background information on extraction of the stated number and motivation for the chosen references.

OEO For the OEO refence used in the main text (*9*) it is not possible to extract material loss of the used cross-linked HLD chromophore as a plasmonic structure was used and plasmonic propagation losses of dB/µm dominate over material loss. The datasheet of HLD states losses of ~ 35dB/cm at 1550 nm (*13*). Note another, chromophore that reports a comparable Pockels coefficient and material losses of 3 dB/cm room temperature (*55*) has been used in Fig. S21. OEO materials with high Pockels but often also high optical losses are especially suitable for applications with short device lengths (i.e. plasmonic or slot waveguides) where their material loss contribution are negligible but currently not for quantum applications.

$LiNbO_3$: Post-fabrication treatments as annealing of thin films fabricated with the "smart cut" technology allows to partially restore the material losses of the bulk resulting in 0.2 dB/m material losses (*12*).

$BaTiO_3$: Propagation loss values were extracted from reference (*8*). However, this reference does not state the material losses explicitly and we provide here a first order estimation with the help of numerical simulations. The propagation losses of SiN waveguide loaded with $BaTiO_3$ and without $BaTiO_3$ are reported as 5.6 dB/cm, 5.4 dB/cm, respectively. Simulating the confinement in both cases, using the heights and geometrical design parameters, yielded a confinement of 0.24 in $BaTiO_3$, 0.33 in SiN and 0.3 in SiN without $BaTiO_3$. As the SiN confinement is almost the same in the case of with or without $BaTiO_3$, the material loss upper limit can be approximated by subtracting the two propagation losses, yielding:

$$\begin{gathered}
\alpha_{prop,\mathrm{BaTiO3}} \approx \frac{5.6dB}{cm} = \Gamma_{BTO}\alpha_{\mathrm{BaTiO3}} + \left(\overbrace{\Gamma_{SiN}}^{0.33}\alpha_{SiN} + \alpha_{scat}\right), \\
\alpha_{prop,no\ \mathrm{BaTiO3}} \approx \frac{5.4dB}{cm} \approx + \left(\overbrace{\Gamma_{SiN}}^{0.3}\alpha_{SiN} + \alpha_{scat}\right), \\
\rightarrow \alpha_{BtO} \leq \frac{\alpha_{prop,BTO} - \alpha_{prop,noBTO}}{\Gamma_{BTO}} \approx 1dB/cm.
\end{gathered} \tag{30}$$

More recently, propagation loss values of ~ 0.1 dB/cm have been reported with a confinement of 63%, yielding a material losses of ~ 0.2 dB/cm (*32*).

Supplementary 7 Optical loss measurement

Optical losses in the $SrTiO_3$ thin film were determined using a cut-back method at room temperature, complemented by substrate loss simulations. Light transmission through a series of PMMA waveguides, with lengths of 5 mm, 10 mm, 15 mm, and 20 mm, was measured using a fiber-to-fiber setup, as illustrated in Fig. S22 A. A tunable laser source, paired with a power meter, was used to investigate the optical properties across wavelengths ranging from 1500 nm to 1625 nm. Single-mode fibers couple light to the chip via grating couplers. To isolate the losses attributable to $SrTiO_3$ from those of PMMA, waveguides were fabricated with different widths of 1.1 µm and 1.7 µm. For each waveguide length, three identical devices were measured. Propagation losses (Fig. S22 C) for both waveguide widths were derived by fitting the transmission data (in dB) at each wavelength using a linear model across the four different lengths. The fitting was validated by correlation coefficient R values above 0.95. Losses from coupling to the Si substrate also contribute to the measured propagation losses. This was verified in Fig. S22 D, which illustrates the cross-sectional mode profile. The trend of the simulated substrate losses as a function of wavelength closely matches the one of the propagation losses. After subtracting the substrate losses, we obtain propagation losses of ~ 2 dB/cm for the 1.7 µm wide waveguides and lower losses of ~ 1.5 dB/cm for the 1.1 µm wide waveguide.

Light confinement within the $SrTiO_3$ is between 35% - 37% using the Poynting vector definition of confinement *(34)* for both widths. Thus, propagation losses should be equally for both types of waveguides. The difference between theory and experiment indicates that other loss mechanism could play a role. For instance, the light confinement within the PMMA increases for larger waveguide widths, which follows the scaling of the losses that increase with larger waveguide width. This would indicate significant loss contribution from the PMMA. However, further experiments with a larger variety of geometrical parameters and thicker SiO_2 substrates are needed to attribute the losses to individual sources. We identify 5.5 dB/cm as an upper material loss limit of the $SrTiO_3$ under the assumptions that 1st) all losses are caused by the $SrTiO_3$ and that 2nd) 37% of light is confined within the $SrTiO_3$.

Fig. S23 A shows a comparison of the 15.37 mm long MZI spectrum at room temperature and 4 K. While the peak of the optimal grating coupler is shifted to the blue for cryogenic temperatures, their power levels are comparable. Additionally, the group refractive index was extracted from the free-spectral range (FSR) of the seven constructive peaks using:

$$\Delta\lambda_{\mathrm{FSR}} = \frac{\lambda_0^2}{n_{\mathrm{g}}\Delta L}, \tag{31}$$

where $\Delta L = 200$ µm is the unbalance in the two arms. For room temperature this yields 1.86 ± 0.1 and for cryogenic 1.84 ± 0.04. A reduction in group refractive index would imply a slightly reduced refractive index and therefore reduced optical material losses according to Kramer-Kronig *(6)*. The reduction for cryogenic could also be explained from the contraction of the PMMA and the reduction of confinement. The comparable power levels and the group refractive indices indicates that no significant loss mechanisms are active at cryogenic temperatures. Due to size constraint mentioned in Supplementary 4.1, no cutback structures could be included in this design. However, another cryogenic measurement of three waveguides with 5 mm length and a MZI with 7.2 mm length was performed. The 2 mm difference in length introduces no strong losses and the power levels of the measurement stay within < 0.5 dB, as shown in Fig. S23 B. Therefore, if material losses increases at cryogenic temperatures, they stay below $(0.5\ \mathrm{dB})/(0.37 \cdot 0.2\ \mathrm{cm}) \approx 7\ \mathrm{dB/cm}$. Further experiments are needed to precisely determine the introduced losses at cryogenic temperatures.

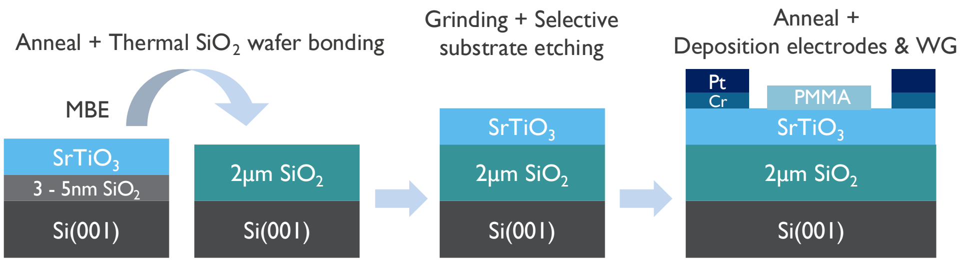

Fig. S1. Illustration of the electro-optic (EO) device fabrication. After $SrTiO_3$ epitaxy on Si (001), the wafer was annealed in oxygen and thermally wafer-bonded onto a SiO_2 box to optically isolate the $SrTiO_3$ film from the silicon substrate. Next, the original Si substrate was removed by grinding and selective substrate TMAH etching. Finally, the film was annealed once more after which the Cr/Pt electrodes and PMMA waveguides were deposited.

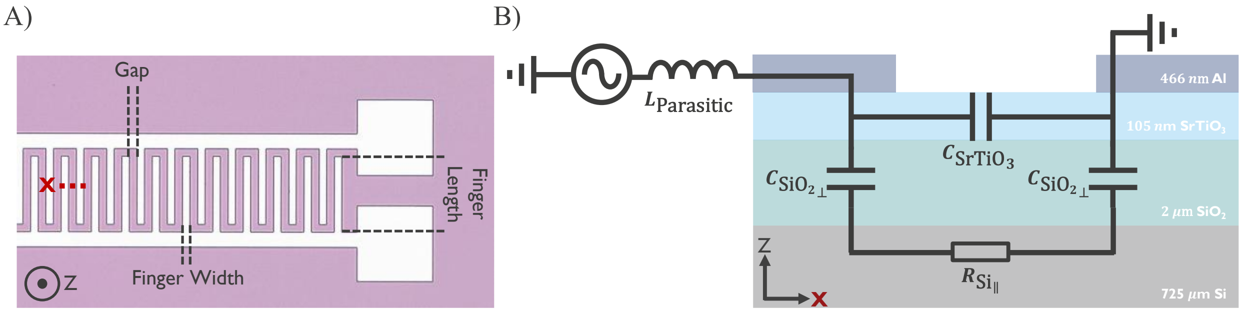

Fig. S2. Interdigitated finger capacitor and electric circuit model. (**A**) Out-of-plane optical microscope image of an IDC capacitor. Geometrical features are annotated, red dashed line shows the representative location of the cross section seen in B). (**B**) Simplified equivalent circuit model considerations including in/out-of-plane capacitances and resistances for the $SrTiO_3/SiO_2/Si$ IDC.

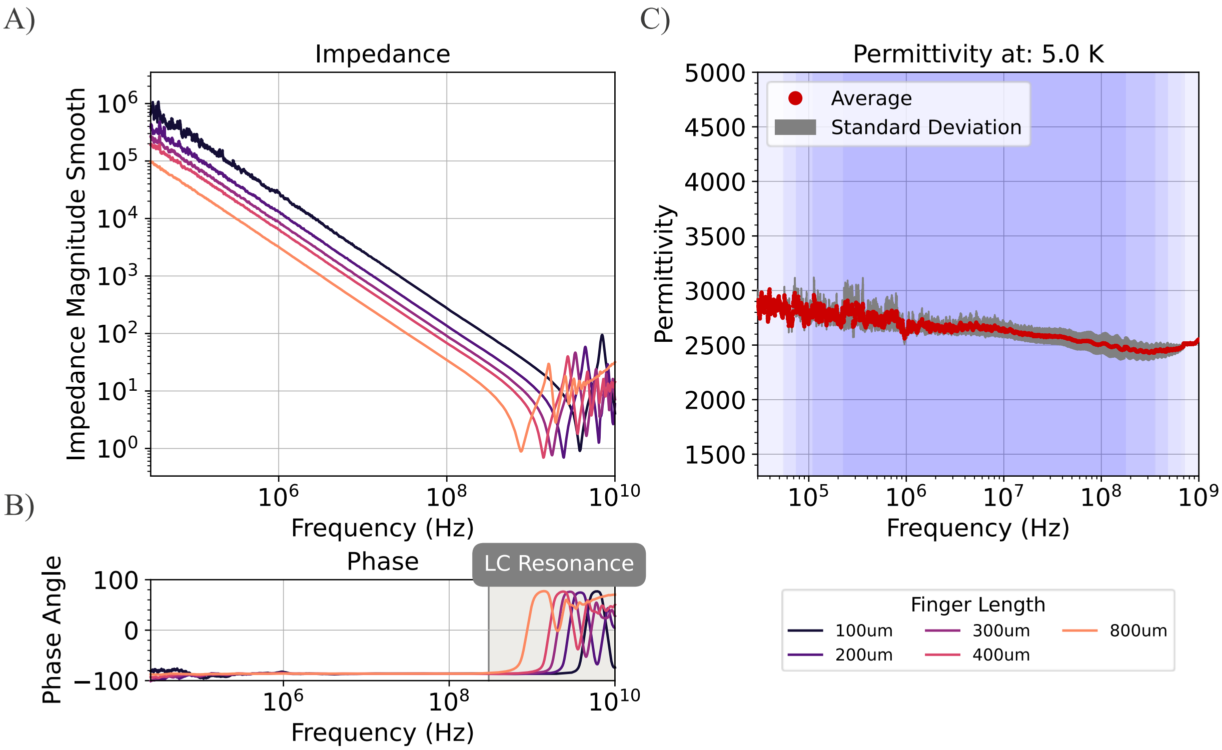

Fig. S3. RF impedance spectroscopy. (**A**) Impedance magnitude and (**B**) phase angle of a subset of capacitors, 4 **µ**m gap and varying finger length (denoted by color in legend), used to extract (**C**) permittivity at 5 K from 30 kHz to 1 GHz. The reduced standard deviation in the highest and lowest frequency regimes arises from the measurement of fewer devices, limited by the frequency range of a particular capacitor. Lightest blue shaded regions represent data obtained with a single device while increasingly darker shaded regions represent an addition of a single device, the darkest region represents the average permittivity of 5 devices.

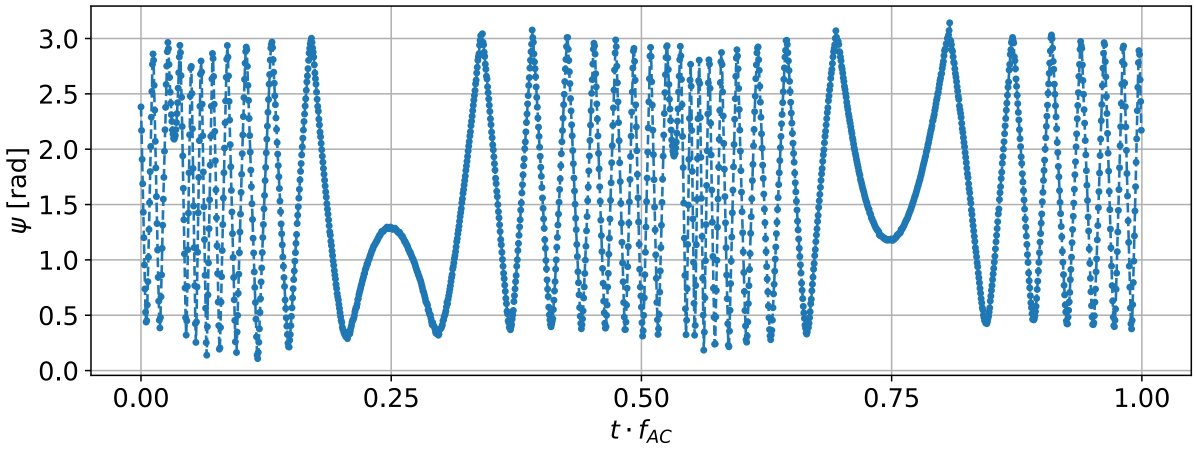

Fig. S4. Electro-optic time domain measurement. Phase vs one electrical modulation period for $\boldsymbol{f_{AC} = 20}$ **Hz**.

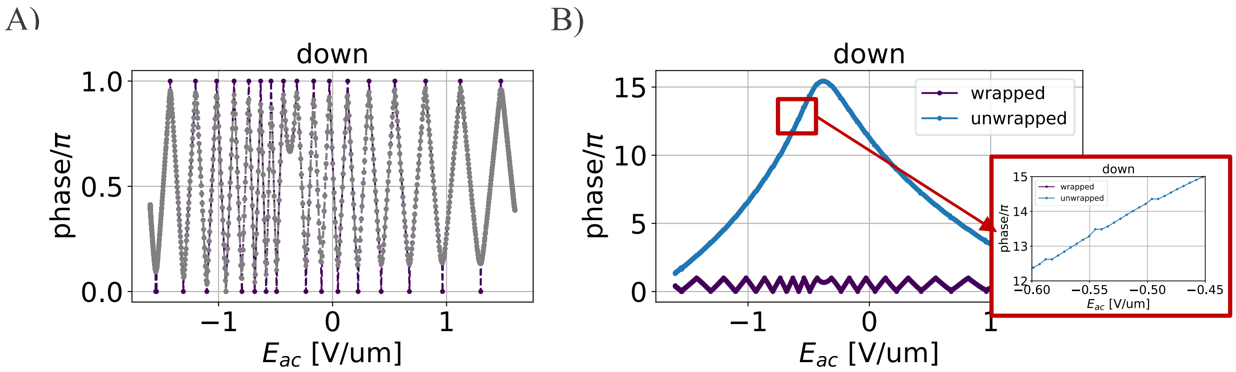

Fig. S5. Phase postprocessing and unwrapping. (A) grey curve shows the raw phase data wrapped. Purple curve shows the turning points extended to 0 or π to compensate low pass-characteristic. **(B)** purple curve is the extended turning points from A). Blue curve is the unwrapped phase response in down direction shown in Fig. 3D. The zoom in shows little peaks from the extension of the turning points which lead to the medium-sized peaks on top of the Pockels coefficient poling curve's envelope due to the numerical implementation of the derivative.

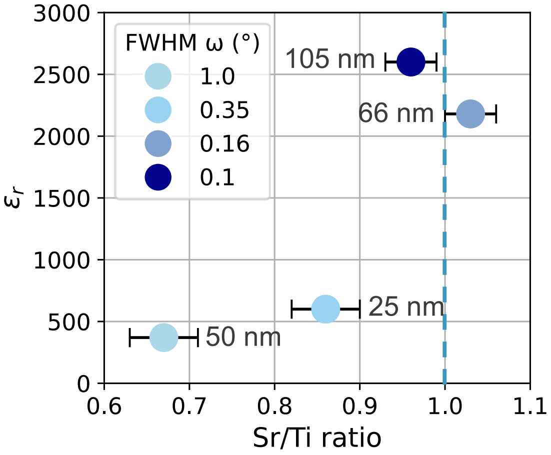

Fig. S6. Cryogenic relative permittivity (ε_r) vs film quality properties. Cryogenic relative permittivity as a function of cationic stoichiometry (Sr/Ti ratio) for four $SrTiO_3$ films with varying thickness and FWHM of the $SrTiO_3$ (002) ω-scan. Sr/Ti near 1 and greater thickness reduce the FWHM and enhance the permittivity.

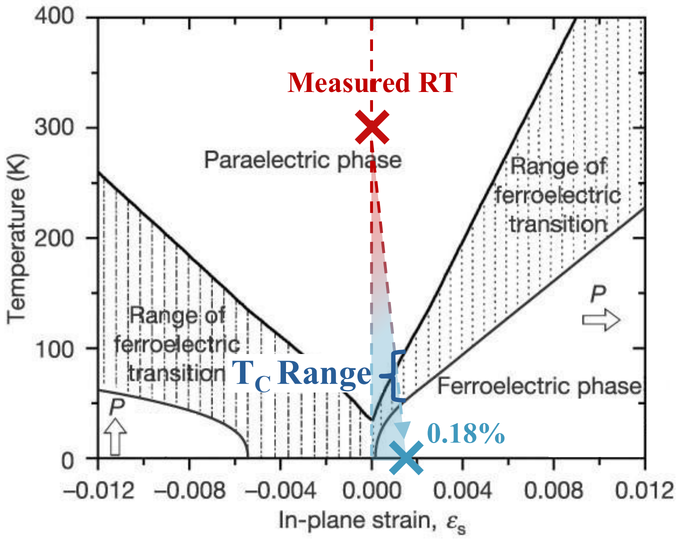

Fig. S7. Phase diagram of bulk $SrTiO_3$. The phase diagram illustrates the relationship between in-plane strain and Curie temperature T_C. At room-temperature, reciprocal space mapping (RSM) indicates a fully relaxed $SrTiO_3$ film, which is consequently in a paraelectric phase (red cross). Relaxed $SrTiO_3$ at 4 K is quantum paraelectric, our upper estimation of 0.18% strain due to the difference in thermal expansion coefficients (CTE) would induce a ferroelectric phase transition (blue cross) with $50 \text{ K} < T_C < 110 \text{ K}$. Figure adapted from (*27*).

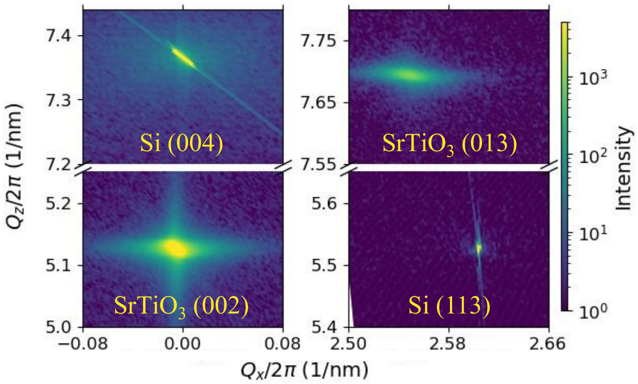

Lattice parameter	**Peak**	
In plane	3.905 Å	± 0.005 Å
Out of plane	3.901 Å	

Fig. S8. XRD analysis. Room-temperature XRD reciprocal space map (RSM) shows the symmetric Si (004) and $SrTiO_3$ (002), and asymmetric Si (113) and $SrTiO_3$ (013) diffraction peaks. The peak positions indicate a fully relaxed cubic $SrTiO_3$ unit cell with lattice parameter equal to bulk (a_{bulk} = 3.905 Å).

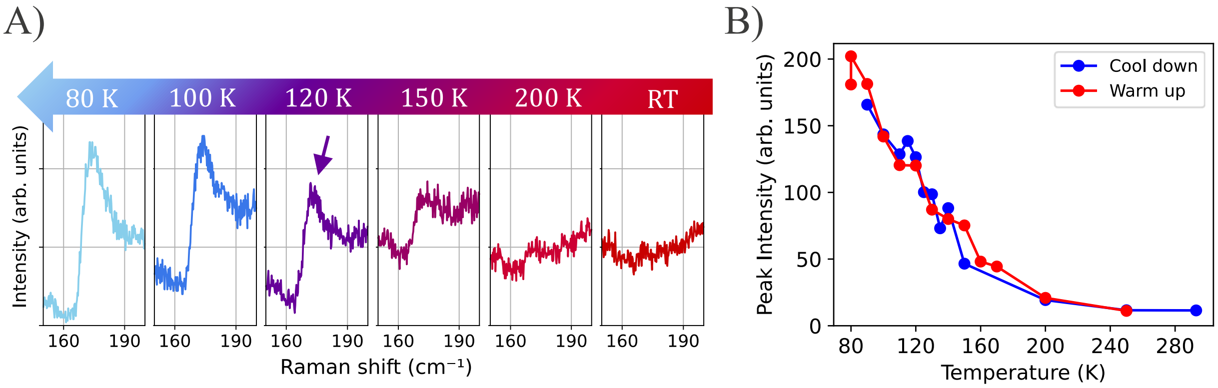

Fig. S9. Raman spectroscopy as indicator of ferroelectricity. (**A**) Appearance of the ferroelectric $SrTiO_3$ phononic mode when cooling down. (**B**) Fitted peak intensity of the mode at 5.2 THz (~ 173 cm^{-1}) as a function of temperature shows the gradual appearance of the Raman signal below 200 K. This behavior is independent whether cooling down or warming up and indicates a relaxor ferroelectric phase.

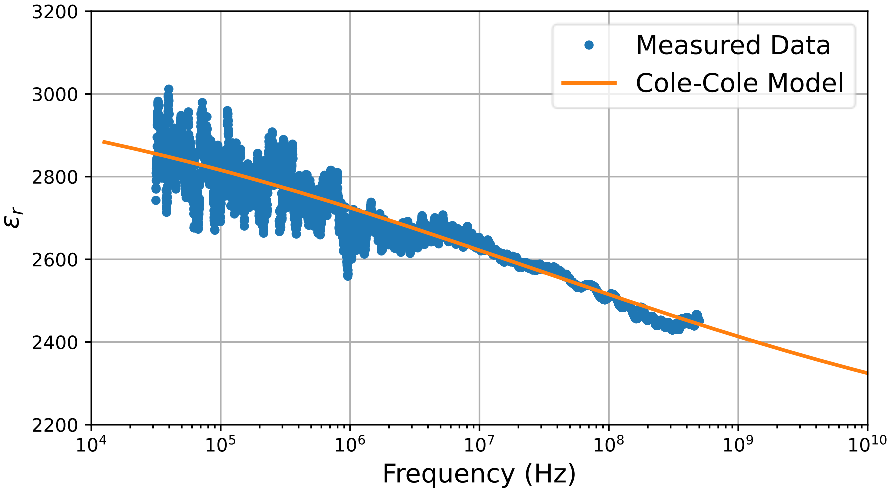

Fig. S10. Fitting of the Cole-Cole model. The behavior of the slightly decreasing relative permittivity ε_r with frequency can be explained by the Cole-Cole relaxation model.

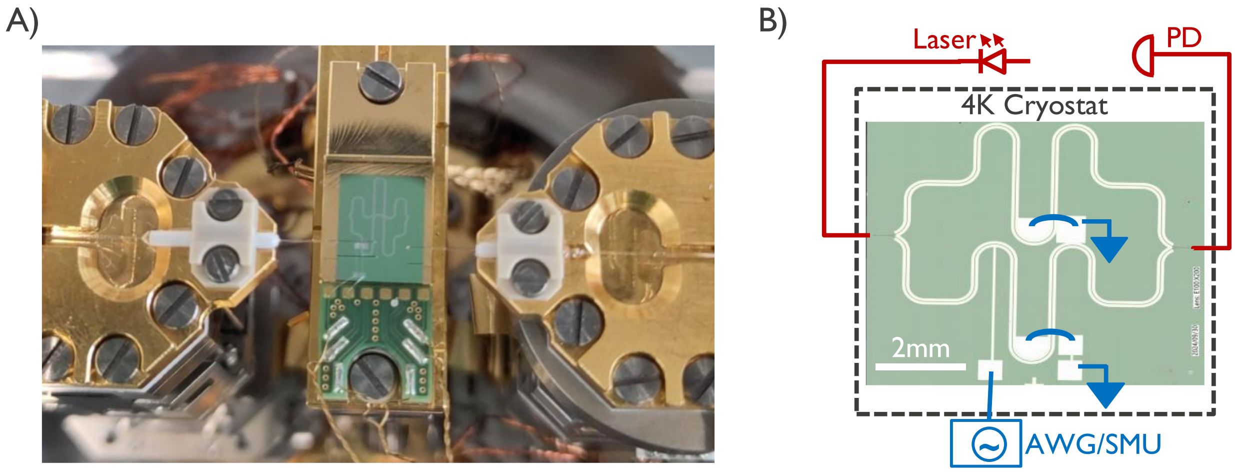

Fig. S11. Electro-optic setup. (**A**) The fibers are mounted with fiber holders onto piezo stages to the left and right of the sample in the center. Angled fibers are used. The sample is silver pasted onto a sample holder and wirebonded to a PCB. The PCB low frequency wires are then connected to the breakout box at the bottom of the cryostat, connecting to the room temperature electronics. (**B**) Setup schematics with laser, photodiode (PD), arbitrary waveform generator (AWG), precision source measure unit (SMU) and zoom in of the MZI sample.

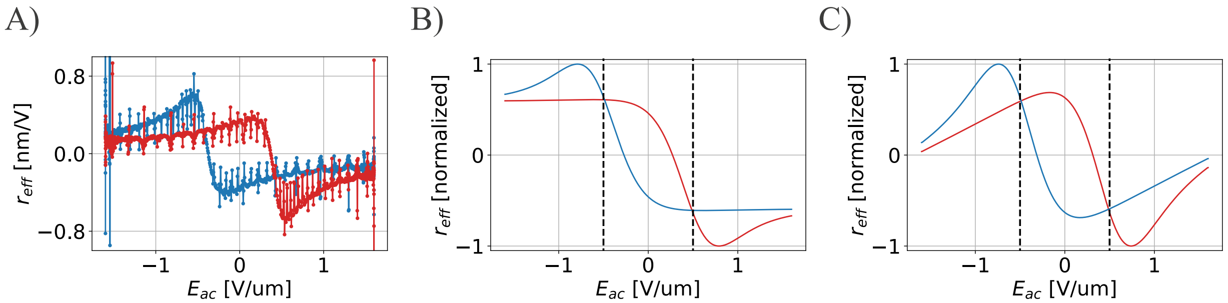

Fig. S12. Comparison of effective Pockels coefficient curve with model. (**A**) Effective Pockels coefficient for up (red) and down (blue) electric field sweep direction. (**B**) Normalized example for $\boldsymbol{r}_{\mathbf{eff}}$ with negligible Kerr coefficient showing a flattening out for field values greater than the coercive field (black dashed vertical line). (**C**) Case for non-negligible Kerr coefficient with same values as in B) showing a linear contribution counteracting $\boldsymbol{r}_{\mathbf{eff}}$.

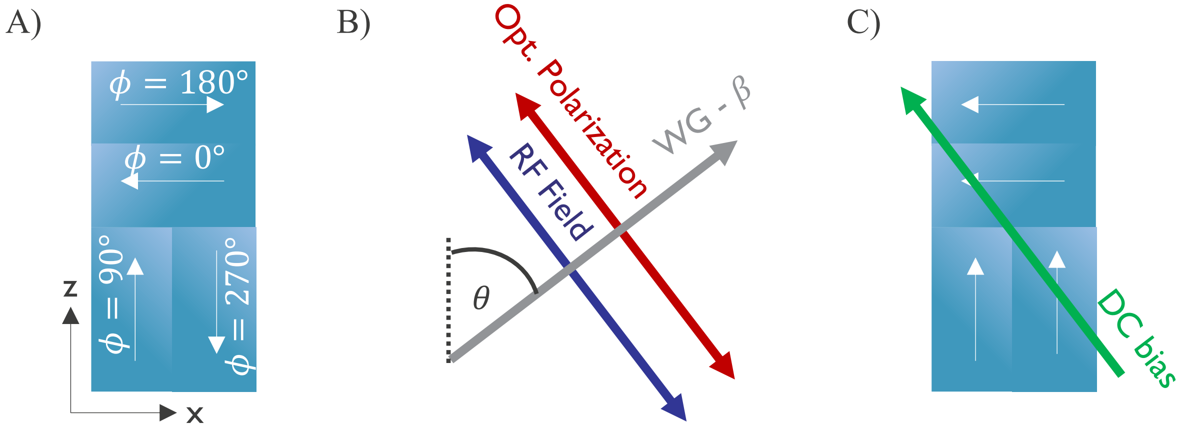

Fig. S13. Concept of crystal domains and poling. (**A**) Schematics of a top view of a-axis film with domains like $BaTiO_3$ or possibly $SrTiO_3$. The white arrow indicates the direction of the spontaneous polarization which is random. For growth reasons, the domains stand perpendicular to each other. (**B**) Illustration of the waveguide orientation (grey) with the optical polarization (red) and the RF field (blue). The electrodes and waveguide run in parallel, aligned at an angle ***θ*** with respect to the crystal domains. (**C**) Schematics of the effect of applying a DC bias and flipping domains resulting in a macroscopic nonzero electro-optic response.

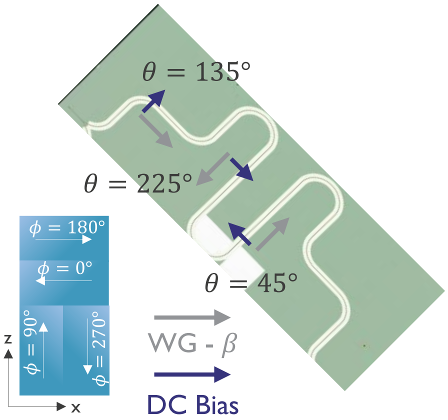

Fig. S14. Schematics of the device and crystal domains. The 45-degree sample is depicted with propagation and DC bias/RF field direction with respect to the z-axis for the different sections of the sample.

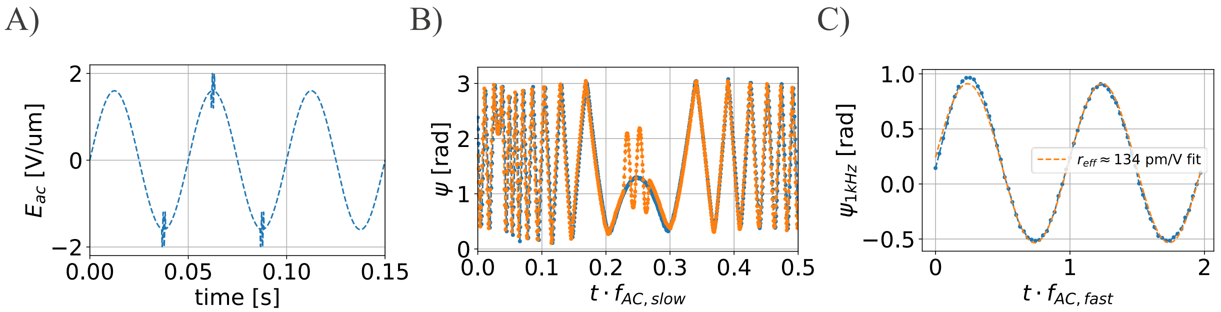

Fig. S15. Small signal Pockels coefficient validation. (**A**) Drive signal composing of $\boldsymbol{f_{\mathrm{AC,slow}} = 20\,\mathrm{Hz}}$ slow signal with 1.6 V/μm amplitude and fast signal with $\boldsymbol{f_{\mathrm{AC,fast}} = 1\,\mathrm{kHz}}$ and 0.05 V/μmamplitude. (**B**) Power signal with and without fast oscillation overlapped and transformed to phase as given by equation (27). (**C**) Subtracted phase signal containing only the 1 kHz contribution with fit.

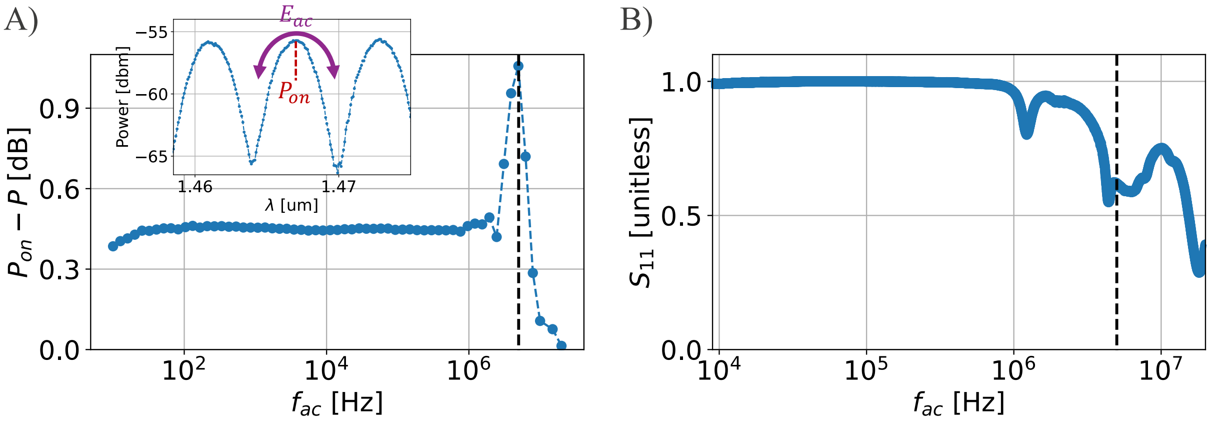

Fig. S16. Electro-optic bandwidth measurement. (**A**) Bandwidth measurement as described in main text up to 20 MHz. The Data shows a resonance peak at 5 MHz (vertical dashed line). (**B**) S11 data of the low frequency lines of our setup without a sample connected (open). The S11 data shows that after 1 MHz the system itself seems to have some intrinsic resonances.

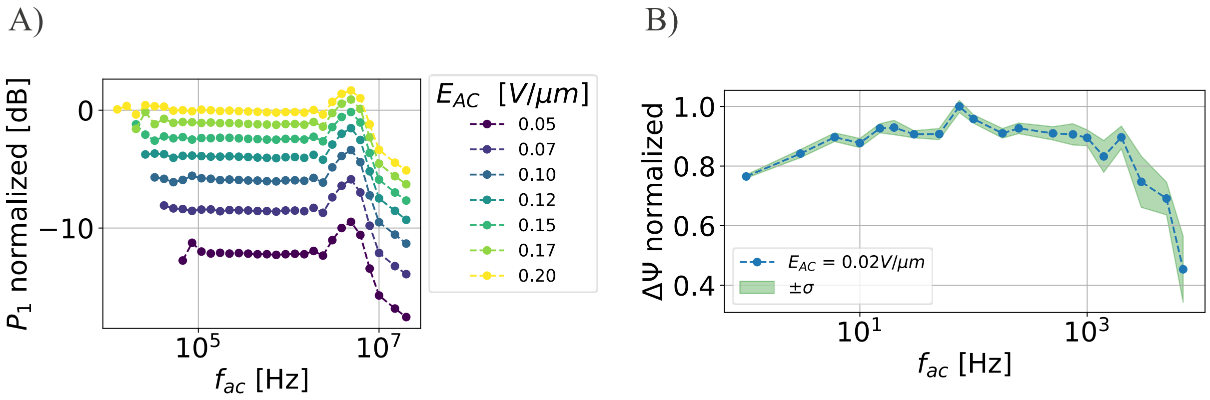

Fig. S17. Additional qualitative bandwidth measurements. (**A**) Bandwidth measurement for different drive voltages using an electrical spectrum analyzer to track the 1st sideband power of the MZI amplitude modulated signal. (**B**) Optical power in time domain measurements for low drive voltage to neglect any poling influence. The phase depicted was extracted using the standard MZI model (equation (8)).

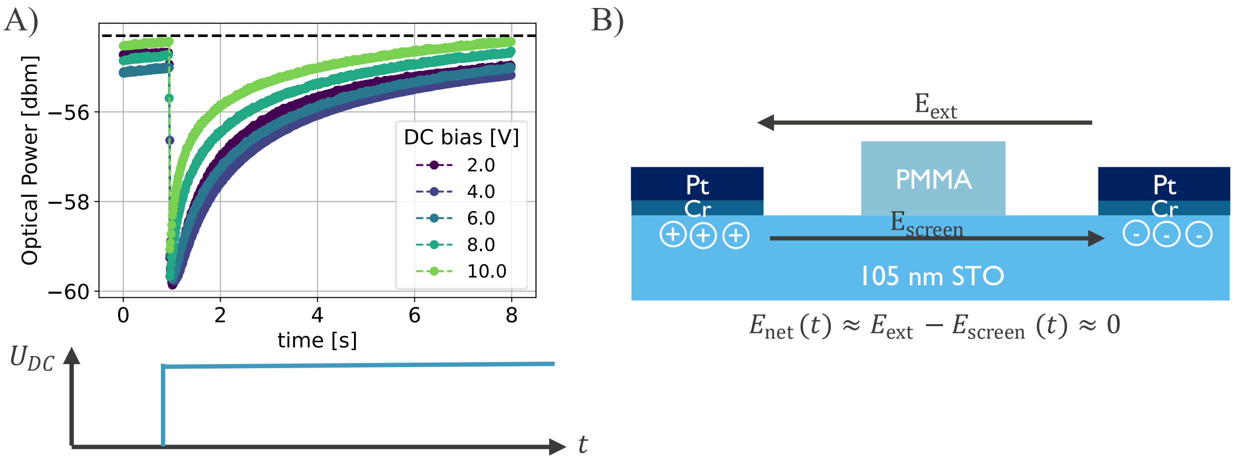

Fig. S18. Illustration of DC screening effect. (**A**) Optical power vs time for different applied DC bias. The DC bias is applied at around t = 1 s and kept constant, as indicated by the plot at the bottom. The measurement shows a clear decay with applied DC bias back to the baseline (indicated by vertical dashed line). Stronger biases decay faster than low biases. (**B**) The hypothesis for the decay of the nonlinear response is the buildup of a screening field within the material, caused by charge carriers like oxygen vacancies.

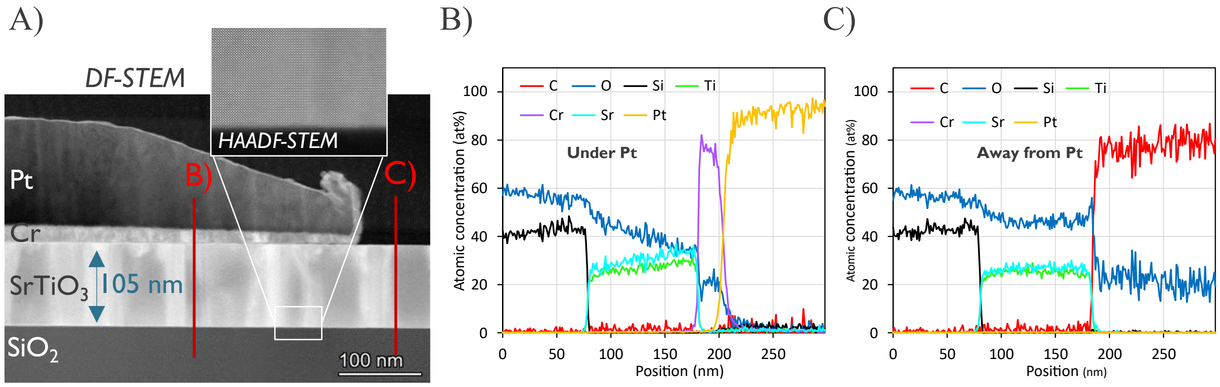

Fig. S19. Oxygen profile comparison. (A) Dark-field STEM image of the material stack at the electrodes of the EO device. Inset shows the HAADF-STEM of the $SiO_2/SrTiO_3$ interface. Red vertical lines show the position of the EDS of B) and C). **(B)** EDS with 30 nm Cr & 140 nm Pt metal contacts. **(C)** EDS without metal. The comparison of the two EDS shows that the oxygen and Sr, Ti profile is not flat as in C), which could be caused by the fully oxidized Cr.

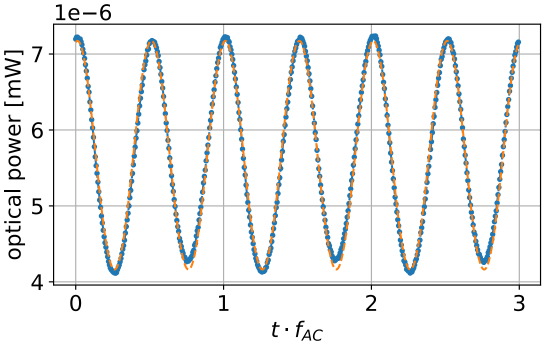

Fig. S20. Room-temperature Kerr coefficient. Optical output power vs three periods of the $\boldsymbol{f_{AC} = 200\ \mathrm{Hz}}$ modulation signal. The dashed line is the fit.

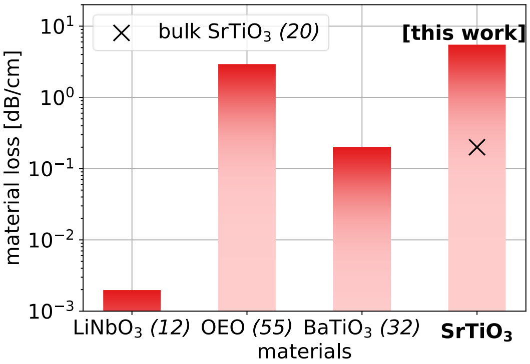

Fig. S21. Comparison of optical material losses of different materials for room temperature at around 1550 nm wavelengths.

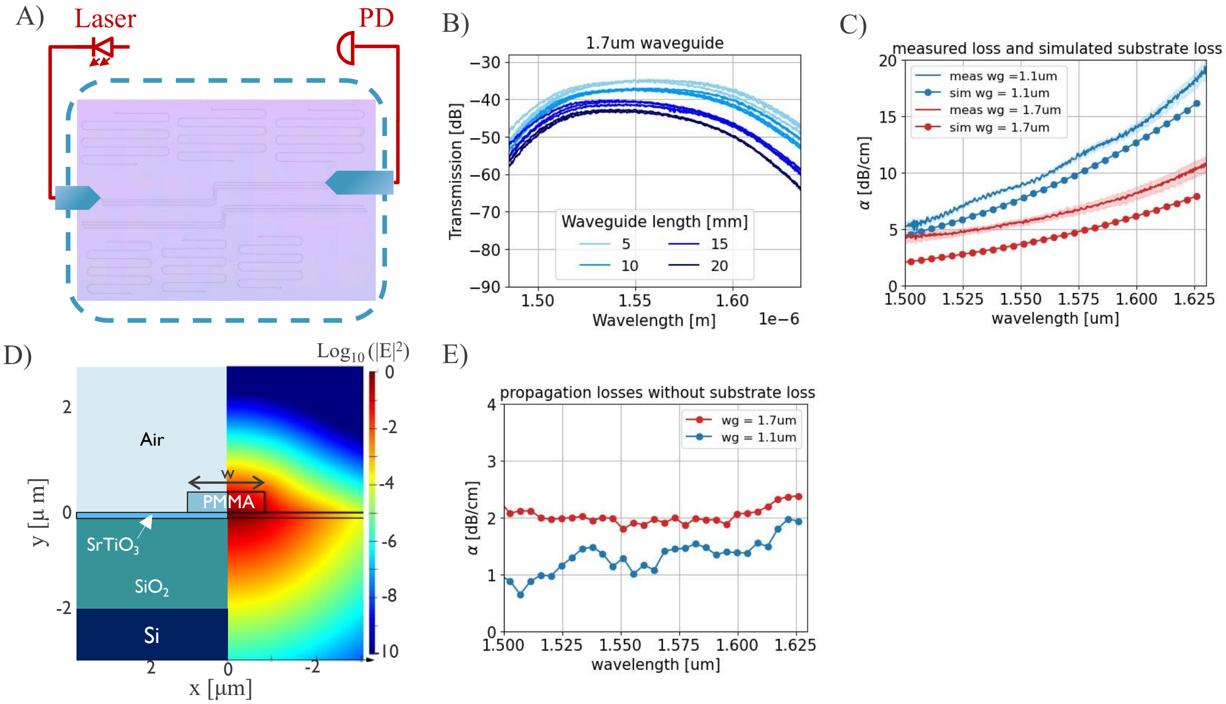

Fig. S22. Room-temperature cutback measurements. (**A**) Schematics of the cut-back measurement setup for optical losses. A tunable laser source, paired with a power meter, is used to measure the transmitted light via PMMA waveguides. (**B**) Result of cut-back measurements for different waveguide lengths with 1.7 um width. (**C**) Measured losses as a function of wavelength for both waveguide widths (shaded area around curves represents the standard deviation). The increasing losses with wavelength can be explained by the contribution of Si substrate losses (dots). (**D**) Cross-sectional mode profile of the $SrTiO_3$ sample, showing the Si substrate contribution. (**E**) Propagation losses after subtracting substrate losses for both waveguide widths have an upper bound of ~ 2 dB/cm.

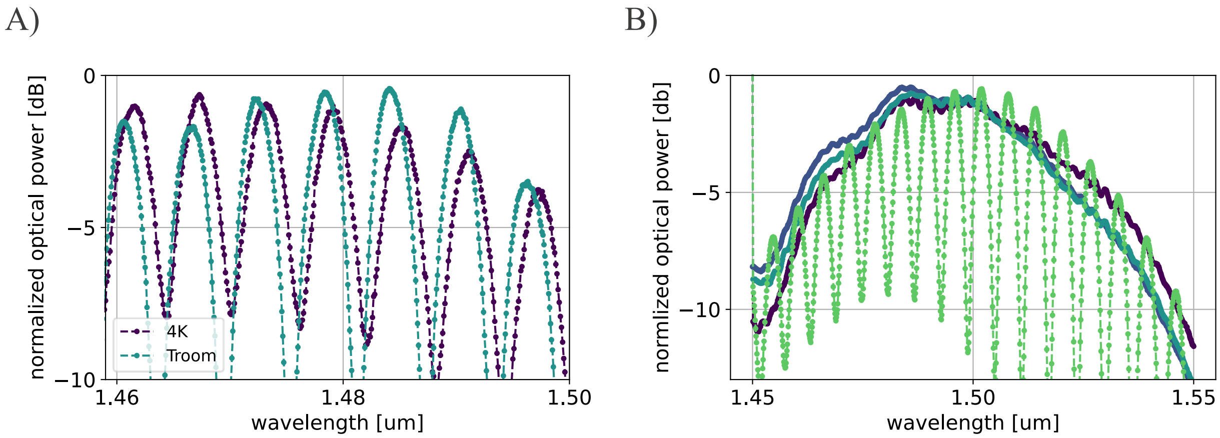

Fig. S23. Comparison optical losses at cryogenic and room temperature. (**A**) Comparison of MZI spectrum at 4 K and room temperature. (**B**) spectra of three waveguide with length of 5 mm (blue to purple) and spectrum of a MZI with arm length of 7.2 mm (green).

$r_{\mathrm{eff}}(\theta)$	$\sigma_{\varphi}\cdot\left(\mathrm{sgn}(v_{\varphi})\cdot\cos\theta\sin^2\theta + \mathrm{sgn}(v_{\varphi})\cdot\sin\theta\cos^2\theta\right)$	r_{eff}
$r_{\mathrm{eff}}(\theta = 45°)$	$0.5\cdot\left((+1)\cdot\left(\frac{1}{2\sqrt{2}}\right)+(+1)\cdot\left(\frac{1}{2\sqrt{2}}\right)\right)$	$1/(2\sqrt{2})\cdot(r_{13}+2r_{51})$
$r_{\mathrm{eff}}(\theta = 225°)$	$0.5\cdot\left((-1)\cdot\left(\frac{-1}{2\sqrt{2}}\right)+(-1)\cdot\left(\frac{-1}{2\sqrt{2}}\right)\right)$	$1/(2\sqrt{2})\cdot(r_{13}+2r_{51})$
$r_{\mathrm{eff}}(\theta = 135°)$	$0.5\cdot\left((-1)\cdot\left(\frac{-1}{2\sqrt{2}}\right)+(+1)\cdot\left(\frac{1}{2\sqrt{2}}\right)\right)$	$1/(2\sqrt{2})\cdot(r_{13}+2r_{51})$

Table S1. Effective Pockels coefficient summarized for the three straight electrode directions given by θ.